



HAL
open science

Mineralogical transformations in polymetallic nodules and the change of Ni, Cu and Co crystal-chemistry upon burial in sediments

Anna Wegorzewski, Sylvain Grangeon, Samuel Webb, Christina Heller,
Thomas Kuhn

► To cite this version:

Anna Wegorzewski, Sylvain Grangeon, Samuel Webb, Christina Heller, Thomas Kuhn. Mineralogical transformations in polymetallic nodules and the change of Ni, Cu and Co crystal-chemistry upon burial in sediments. *Geochimica et Cosmochimica Acta*, 2020, 282, pp.19-37. 10.1016/j.gca.2020.04.012 . hal-03740008

HAL Id: hal-03740008

<https://brgm.hal.science/hal-03740008>

Submitted on 5 Dec 2022

HAL is a multi-disciplinary open access archive for the deposit and dissemination of scientific research documents, whether they are published or not. The documents may come from teaching and research institutions in France or abroad, or from public or private research centers.

L'archive ouverte pluridisciplinaire **HAL**, est destinée au dépôt et à la diffusion de documents scientifiques de niveau recherche, publiés ou non, émanant des établissements d'enseignement et de recherche français ou étrangers, des laboratoires publics ou privés.

Mineralogical transformations in polymetallic nodules and the change of Ni, Cu and Co crystal-chemistry upon burial in sediments

Anna V. Wegorzewski^a, Sylvain Grangeon^b, Samuel M. Webb^c, Christina Heller^a, and Thomas Kuhn^a

^a Federal Institute for Geoscience and Natural Resources (BGR), Stilleweg 2, D-30655 Hannover, Germany. Anna.Wegorzewski@bgr.de

^b BRGM, 3 Avenue Claude Guillemin, 45060 Orléans cedex 2, France

^c Stanford Synchrotron Radiation Laboratory, Menlo Park, California 94025, U.S.A.

Abstract

Polymetallic nodules from the Clarion-Clipperton Zone of the equatorial Pacific Ocean were studied using X-ray diffraction, X-ray absorption, Fourier-transformed infrared spectroscopy and transmission electron microscopy. This study includes nodules found at the sediment surface as well as subsurface (14-16 cm sediment depth) and deeply buried (530-985 cm sediment depth) nodules. The surface and subsurface nodules are currently under oxic conditions whereas the deeply buried nodules are under suboxic conditions. Surface nodules consist mainly of turbostratic phylломanganates (7 Å and 10 Å vernadite and Fe-vernadite); todorokite is a minor phase, if present at all. In contrast, subsurface and especially deeply buried nodules predominantly consist of todorokite, which increases in abundance with depth in the sediment. Thus, upon burial of nodules within the shallow sediment, phylломanganates transform to todorokite, probably through the combined action of time and change in the ambient chemical conditions. Nodules from deeper sediment depth (>500 cm) consist primarily of todorokite and additionally show signs of dissolution.

The transformation of phylломanganates to todorokite and their further dissolution upon nodule burial under suboxic conditions induces modifications in the crystal-chemistry of Ni, Co, and Cu. In surface nodules, Ni and Co are incorporated in the octahedral sheets of phylломanganates, whereas Cu is located at the crystal edges of those phylломanganate sheets. In buried nodules Cu and to a lesser extent Ni are incorporated in todorokite by forming outer-sphere complexes within the tunnels. However, Ni is predominantly

32 incorporated within the octahedra of the newly formed todorokite structure. Co is also
33 enriched in the octahedra of todorokite as a result of dissolution of hydrogenetic vernadite and
34 re-incorporation in the more stable Mn-phases formed during the diagenetic transformation.
35 Co enrichment under suboxic conditions after burial within the sediments is noteworthy since
36 Co in surface nodules is characteristic for oxic conditions.

37

38 **Keywords:** *manganese nodules, phylломanganate, todorokite, hydrogenetic, suboxic-diagenetic,*
39 *cobalt, nickel, copper, XRD, IR, EXAFS*

40

41 **1. INTRODUCTION**

42 Manganese (Mn) nodules are Mn-Fe oxy-hydroxide concretions occurring in almost all
43 oceans, at water depths between approximately 3000 and 6000 m (e.g., Halbach et al., 1988;
44 Koschinsky and Halbach 1995, Hein et al., 2013; Kuhn et al., 2017a). Mn-nodules are
45 potential resources for Fe, Mn, Ni, Cu, Co, Zn, Mo as well as rare earth elements (REE; e.g.,
46 Halbach et al., 1988; Hein et al., 2013; Hein and Koschinsky, 2013).

47 In general, Mn-nodules form on the sediment surface or within the first few centimeters of the
48 sediment (Halbach et al., 1988). They are made up of individual nm- to μm -thick layered
49 growth structures (LGS), which grow around a nucleus (e.g., rock fragments, shark teeth;
50 Halbach et al., 1988). Individual LGS are the result of hydrogenetic (oxic) and/or suboxic-
51 diagenetic precipitation.

52 Hydrogenetic LGS form by Mn and Fe precipitation from oxygen-rich seawater (oxic;
53 Halbach et al., 1988; Koschinsky and Halbach 1995) as well as from oxic sediment pore water
54 (Wegorzewski and Kuhn 2014; Kuhn et al., 2017a). Oxic diagenesis is characterized by redox
55 potentials of around +490 mV, the presence of oxygen, low amounts of dissolved manganese
56 (few $\mu\text{g}\cdot\text{l}^{-1}$) and nitrate formation within the environment (nitrification; Halbach et al., 1988).

57 Hydrogenetic LGS generate dense layers with columnar growth structures and are
58 characterized by Mn/Fe ratios of <4 as well as low Ni (0.46 ± 0.24 wt.%) and Cu (0.34 ± 0.16
59 wt.%) contents, but high Co (0.30 ± 0.12 wt.%) and REE (~ 800 ppm) contents (Halbach et al.,
60 1988; Wegorzewski and Kuhn 2014; Kuhn et al., 2017a). The preferential association of a
61 given element with Mn or Fe oxide phases might result from its aqueous speciation, as Mn
62 oxides are generally negatively charged under sea water conditions, whereas Fe oxy-
63 hydroxides are neutral or slightly positively charged (Koschinsky and Halbach 1995).
64 Mineralogically, hydrogenetic LGS consist of turbostratic Fe-vernadite ($\delta\text{-MnO}_2$) that is

65 epitaxially intergrown with an amorphous δ -FeOOH phase (Koschinsky and Halbach 1995;
66 Hein et al., 2013; Wegorzewski et al., 2015).

67 Suboxic-diagenetic LGS are formed by metal precipitation from suboxic near-bottom sea
68 water and/or sediment pore water (Halbach et al., 1988; Koschinsky and Halbach 1995;
69 Wegorzewski and Kuhn 2014). The suboxic conditions for LGS formations are characterized
70 by low or even zero oxygen concentrations ($<5 \mu\text{mol O}_2 \cdot \text{l}^{-1}$; Hein and Koschinsky 2014), a
71 redox potential of around +330 mV, nitrate reduction (denitrification), and the occurrence of
72 dissolved manganese (Halbach et al., 1988). Under these suboxic conditions, Mn^{4+} can be
73 reduced but no Fe^{3+} reduction and dissolution occurs. Suboxic-diagenetic LGS have Mn/Fe
74 ratios of 5 – 800, Ni and Cu amounts reaching up to ~4 wt.%, but low Co (0.08 ± 0.08 wt.%)
75 and REE (<600 ppm) concentrations (Koschinsky and Halbach 1995; Wegorzewski and Kuhn
76 2014; Kuhn et al., 2017a). Mineralogically, they consist of 7 Å and 10 Å vernadite, where the
77 numbers refer to the phylломanganate layer-to-layer distance. Occurrences of todorokite in
78 marine Mn-nodules from the sediment surface of the Clarion and Clipperton Zone (CCZ) are
79 scarce (e.g., Manceau et al., 2014; Wegorzewski et al., 2015; Bodeř et al., 2007; Manceau et
80 al., 2014; Atkins et al., 2016).

81 Studying the mineralogy of marine Mn-nodules (Burns and Burns, 1978a; Manceau et al.,
82 2014; Peacock and Sherman, 2007a,b; Peacock 2009) is difficult, because the minerals are
83 poorly crystalline, intermixed with each other on a nm scale (Burns and Burns 1977; Usui and
84 Terashima, 1997; Atkins et al., 2016), and have overlapping diffraction peaks (Post and Bish,
85 1988; Bodeř et al., 2007; Manceau et al., 2014). Additional complexity results from the
86 topotactic relation between phylломanganates and todorokite (Bodeř et al., 2007; Pal'chick et
87 al., 2011; Manceau et al., 2014).

88 The chemical and mineralogical composition of individual LGS reflects the environmental
89 conditions within which the nodules grew (e.g., Wegorzewski and Kuhn, 2014; Koschinsky
90 and Hein, 2017). However, secondary transformation of primary LGS over time may also
91 occur (Wegorzewski and Kuhn, 2014; Blöthe et al., 2015). Indeed, because of the high
92 porosity (up to 60%) and permeability of the nodules (Blöthe et al., 2015), surrounding water
93 can penetrate the nodules and induce mineralogical changes if the water chemistry changes
94 with time (for example as a result of climate cycles).

95 Nodules do not only occur on the sediment surface, but they are also found buried within the
96 sediment column. Buried nodules have been sampled sporadically in the Pacific, Atlantic and
97 Indian Oceans (Cronan and Tooms, 1967; Banerjee et al., 1991; Heye et al., 1979; Pattan and
98 Parthiban, 2007). Heller et al., (2018) documented the occurrence of buried nodules down to

99 ~10 m sediment depth within siliceous ooze of the eastern CCZ in the central Pacific Ocean.
100 The authors distinguished between nodules buried at shallow depth (subsurface nodules; <
101 100 cm) currently under oxic conditions and nodules buried at greater depths (deeply buried
102 nodules; > 500 cm) currently under suboxic conditions (Heller et al., 2018).
103 Nodules buried within the sediment column differ from surface ones in the occurrence of
104 individual LGS as well as in their chemical composition (Heller et al., 2018). Compared to
105 surface nodules, buried nodules are depleted in Ni, Zn, Mo, and Li whereas they are enriched
106 in Co, W, and Te. Mn, Cu, V, and Ba have about the same concentration in both types of
107 nodules (Heller et al., 2018). Furthermore, there is an additional type of layer growth structure
108 in buried nodules that has not been found in surface nodules. This growth structure has high
109 contents of Fe and is rich in Si and Al, but has low trace metal concentrations (Heller et al.,
110 2018). The fate of nodules during their burial process is unclear. Do nodules continue to grow
111 further, stop growing, or do they dissolve? Heller et al., (2018) showed that Mn-nodules
112 buried in suboxic deep-sea sediments are subject to diagenetic processes induced by reactions
113 with the surrounding pore water. These diagenetic processes affect the geochemical
114 composition of the nodules as well as the surrounding sediments (Heller et al., 2018). The
115 results of this study are the continuation of the previous work by Heller et al., (2018), but
116 focus on the mineralogy and the crystal-chemistry of Ni, Cu, and Co in nodules from the
117 sediment surface in comparison with buried ones. The overall aim of this study is to
118 determine how Mn minerals and associated metals evolve with time and burial.

119

120 **2. MATERIAL AND EXPERIMENTAL METHODS**

121 **2.1 Material**

122 Samples were recovered during RV *SONNE* cruises SO205 (in 2010) and SO240 (in 2015)
123 within the eastern Clarion and Clipperton Zone in the Pacific Ocean (Rühlemann et al., 2011;
124 Kuhn et al., 2015). Figure 1 shows a bathymetric map of the study area with sample locations
125 (Kuhn et al., 2015). Samples were collected from the sediment surface (using a box corer
126 (KG); SO205-32KG, SO205-44KG, SO205-68KG, SO240-21KG) in water depths between
127 4200 and 4500 m (Rühlemann et al., 2011; Kuhn et al., 2015), as well as from different
128 sediment depths using a box corer (SO240-107KG-16cm), piston corer (KL: SO240-09KL-
129 14-16cm, SO240-22KL-530cm, SO240-22KL-801cm, SO240-09KL-837cm), and gravity
130 corer (SL: SO240-65SL-985cm). Buried nodules were collected in sediment cores that were
131 taken where hydroacoustic data showed a change in the density of the sediment between 500

132 and 1000 cm depth (BGR data; Rühlemann et al., 2018). Detailed descriptions of the study
133 area can be found in Rühlemann et al. (2011; 2018) and Kuhn et al. (2015). Different nodule
134 types (surface nodules, subsurface nodules (<100 cm) and deeply buried nodules (>500 cm;
135 Heller et al., 2018)) were chosen for further detailed mineralogical and crystal-chemical
136 investigations. For a more detailed description of the chemistry of the buried nodules see
137 Heller et al. (2018).

138

139 **2.2 Electron probe microanalyzer (EPMA)**

140 Chemical mappings were performed with an electron probe microanalyzer (EPMA: JEOL
141 JXA-8530F). Samples were prepared as polished thin sections (~50 µm thick). Manganese,
142 Fe, Ni, and Cu were mapped using energy dispersive X-ray spectrometry and Co using
143 wavelength-dispersive X-ray spectrometry (WDX). The beam size was 3-5 µm and the dwell
144 time was 500 ms. The accelerating voltage was set to 15 kV and a beam current of 20 nA was
145 used. In addition to the mapping, individual point analyses were conducted to better quantify
146 metal contents of individual growth structures. For a detailed description of the EPMA
147 measurements see Wegorzewski and Kuhn (2014).

148

149 **2.3 X-ray diffraction (XRD)**

150 Mineralogy was determined for three bulk nodules from the sediment surface (44KG, 68KG,
151 21KG-1), three nodules from the subsurface (107KG-16cm, 107KG-36cm; 09KL-14-16cm)
152 and four nodules from greater sediment depths (22KL-530cm, 22KL-801cm, 09KL-837cm,
153 65SL-985cm).

154 Nodules were cut in half and one complete half was ground in a planetary sphere mill (Retsch
155 PM 11 CM; ≤50 µm particle size). Powder XRD patterns were collected using a PANalytical
156 X'Pert PRO MPD θ-θ diffractometer (Cu-Kα radiation generated at 40 kV and 30 mA),
157 equipped with a variable divergence slit (20 mm irradiated length), primary and secondary
158 soller slits, Scientific X'Celerator detector (active length 2.122°; phd 60), and a sample
159 changer (sample diameter 26 mm). Samples were scanned over 5° to 85° 2θ with a step size
160 of 0.0334° 2θ and a measuring time of 200 sec per step.

161 To distinguish between todorokite and 10 Å phyllosulfates, nodule powder was analyzed
162 twice, after drying at 40°C and after drying at 105°C (Uspenskaya et al., 1987; Manceau et
163 al., 2014). Upon drying at 105°C, 10 Å phyllosulfates such as busserite loose interlayer

164 water and collapse, thus reducing the layer-to-layer distance and the corresponding diffraction
165 peak to ~ 7 Å. In contrast, the 10 Å reflection of todorokite remains unchanged upon heating
166 at 105 °C.

167

168 **2.4 Transmission electron microscopy (TEM)**

169 Slices from layers of buried nodule 22KL-801cm were cut using a focused ion beam
170 preparation technique (FIB) at the GeoForschungsZentrum, Potsdam (Wirth; 2009). Different
171 growth structures of interest were selected for sampling based on EPMA analyses. The
172 sampled foils (15 x 10 x 0.150 µm) were sputtered from the target material using Ga-ions
173 with energy of 30 keV (Wirth; 2009). For high-resolution transmission electron microscopy
174 foils were taken from the excavation sites applying the so-called lift-out technique (Giannuzzi
175 et al. 1997). Detailed description of the FIB technique is given in Giannuzzi et al. (2005) and
176 Wirth (2004; 2009). TEM analyses were carried out using a Philips CM20 operated at 200
177 kV.

178

179 **2.5 Extended X-ray absorption fine structure (EXAFS) spectroscopy**

180 EXAFS experiments were conducted at the Stanford Synchrotron Radiation Lightsource
181 (SSRL). Ni and Cu *K*-edge X-ray absorption spectroscopy was carried out on bulk nodules
182 [surface nodules, subsurface nodules (14 – 16cm) and deeply buried nodules (530 – 985cm)].
183 Ni and Cu *K*-edge EXAFS analyses of bulk nodules (powder samples) were performed at
184 beam line 4-1 using a Si (220) double crystal monochromator calibrated to 8979 eV with a
185 Cu(0) foil and to 8333 eV with a Ni(0) foil. Sample powders were fixed to polyimide tape on
186 the sample holder. X-ray absorption spectra were averaged before analysis for better statistics.
187 Co *K*-edge EXAFS analyses were performed on thin sections at beam line 10-2. High-
188 resolution XRF maps were collected prior to EXAFS measurements to identify regions of
189 interest. Additional Co *K*-edge X-ray absorption spectroscopy was carried out on different
190 individual Co rich areas of suboxic-diagenetic LGS in one deep buried nodule (22KL-801cm).
191 X-ray absorption data for Co were recorded over the energy range of 7479 to 8315 eV. The
192 incorporation mechanism of Co in vernadite (δ -MnO₂) within hydrogenetic LGS of surface
193 nodules has been thoroughly studied (e.g., Manceau et al., 2014) and was not determined in
194 this study. Individual Co EXAFS spectra were averaged together to improve counting
195 statistics as they were noted to have similar features.

196 The storage ring energy during the measurements was 3.0 GeV and the beam current was
197 maintained at ~500 mA in top-off mode. The X-ray absorption spectra were normalized using
198 the software Athena and the EXAFS spectra were Fourier-filtered afterwards (Ravel and
199 Newville, 2005). The EXAFS spectra were k^3 -weighted and converted to R-space by fast
200 Fourier transformation over the k range of 2.5-12 \AA^{-1} using a Kaiser-Bessel window with the
201 windowing parameter (dk) set to 3 \AA^{-1} (Peña et al., 2015).

202

203 **2.6 Fourier-transformed infrared spectroscopy (FTIR)**

204 Mid- (MIR) and far- (FIR) infrared spectra were collected on pellets made of 1 mg of sample
205 mixed with 200 mg of KBr. The analyses were conducted on a Thermo Nicolet Nexus FTIR
206 spectrometer (MIR beam splitter KBr, detector DTGS TEC; FIR beam splitter solid substrate,
207 detector DTGS PE) at the BGR laboratory. The resolution was adjusted to 2 cm^{-1} .

208

209 **3. RESULTS**

210 **3.1 Element associations in surface and buried nodules**

211 EPMA maps show different Ni, Cu, and Co associations in surface (e.g., 32KG) and deeply
212 buried nodules (e.g., 22KL-801cm; Figs. 2a-f and 3a-f). In nodules from the sediment surface,
213 two types of LGS can be recognized: one is enriched in Mn (20 - 51 wt.%) and depleted in Fe
214 (0.5 - 3 wt.%), and the other is enriched in Fe (4 - 23wt.%) and has Mn concentrations
215 ranging from 7 to 37 wt.% (Fig. 2b,c). Ni and Cu are enriched in Mn-rich LGS, which is
216 typical for suboxic-diagenetic growth (Fig. 2a,d,e; Halbach et al., 1988; Wegorzewski and
217 Kuhn, 2014). LGSs showing columnar growth and low reflectivity (Fig. 2a) are enriched in Fe
218 (~17 wt.%) as well as Mn (~23 wt.%; Fig. 2d,e). This type of LGS is typical of hydrogenetic
219 growth, and those layers are enriched in Co (0.3 wt.%; Fig. 2f), but depleted in Ni (~0.4
220 wt.%) and Cu (~0.3 wt.%). This metal association is systematically observed in all surface
221 nodules from the eastern German license area within the CCZ (Wegorzewski and Kuhn,
222 2014).

223 In addition to the hydrogenetic and suboxic-diagenetic LGS, deeply buried nodules (e.g.,
224 22KL-801cm) contain another LGS of low reflectivity (Fig. 3a) that is enriched in Fe (14
225 wt.%), Si (20 wt.%) and Al (2.2 wt.%) but depleted in Mn (0.5 wt.%; Fig. 3b,c; also Heller et
226 al., 2018). Detailed investigations here show that this LGS is not homogenous but rather a

227 mixture of different materials, Fe-Si rich material is mixed with hydrogenetic material (Fig.
228 4).

229 In deeply buried nodules, Cu (0.6 – 1.8 wt.%) as well as Ni (0.3 – 2.3 wt.%) are still strongly
230 associated with Mn within the suboxic-diagenetic LGS (Fig. 3b,d,e). In contrast to surface
231 nodules, Co is also enriched in suboxic-diagenetic LGS (Co 0.2 – 1.2 wt.%; Fig. 3f), and the
232 hydrogenetic layers (0.3 wt.%; Halbach et al., 1988; Wegorzewski and Kuhn 2014). Co, Cu,
233 and Ni are unevenly distributed within the suboxic-dendritic LGS as in surface nodules but
234 are predominantly enriched at the rim of the LGS in contact with the pores and the Fe-rich
235 LGS (Fig. 3d-f).

236

237 **3.2 Mineralogy**

238 **3.2.1 XRD and TEM**

239 The XRD patterns of surface, subsurface and deeply buried nodules are shown in Fig. 5. The
240 patterns of surface nodules have diffraction peaks at $\sim 10 \text{ \AA}$ (assigned to be the 001 reflection)
241 and $\sim 5 \text{ \AA}$ (002 reflection of the same mineral) as well as weak peaks at $\sim 7 \text{ \AA}$ (001 reflection
242 of another mineral) and $\sim 3.5 \text{ \AA}$ (002 reflection of this second mineral). Furthermore, two *hk*
243 bands at $\sim 2.45 \text{ \AA}$ (10 band) and $\sim 1.42 \text{ \AA}$ (11 band) can be distinguished. This pattern is
244 typical for turbostratic phyllosilicates. The layer symmetry of this mineral is hexagonal as
245 the calculated ratio of the *d*-spacings of the two *hk* bands is ~ 1.73 (close to $\sqrt{3}$) and the band
246 at 1.42 \AA is almost symmetrical (e.g., Drits et al., 1997; Bodeř et al., 2007; Drits et al., 2007).
247 Since the 002 reflection is of lower intensity than the 001 reflection, the presence of
248 significant amounts of asbolane is unlikely.

249 Buried nodules (subsurface and deeply buried nodules) show diffraction peaks at $\sim 10 \text{ \AA}$ and
250 $\sim 5 \text{ \AA}$, which are sharper and of higher intensity (especially for the deeply buried nodules) than
251 those of the surface nodules. The 7 \AA reflection is much weaker compared to nodules from the
252 surface and in some samples this reflection is almost absent (e.g., 09KL-837cm in Fig. 5).
253 Furthermore, in buried nodules, a splitting of the *hk* band around 2.45 \AA ($\sim 2.45 \text{ \AA}$ and ~ 2.40
254 \AA) is observed, and additional reflections are observed between 2.2 and 1.5 \AA . The $\sim 2.45 \text{ \AA}$
255 and $\sim 2.40 \text{ \AA}$ peaks are more intense in deeply buried nodules than in subsurface nodules.
256 Other sharp peaks match the patterns of different minerals such as quartz, feldspars and
257 phillipsite (Fig. 5).

258 After drying the samples at $105 \text{ }^\circ\text{C}$, the $\sim 10 \text{ \AA}$ reflection of surface nodules decrease,
259 concomitant with an increase of the 7 \AA peak. Only a small broad hump remains around $\sim 9 \text{ \AA}$,
260 if at all. The *hk* bands are unaffected by drying (e.g., 21KG; Fig. 5). These results confirm that

261 the ~ 10 Å phase of surface nodules is mainly, if not purely, a turbostratic phylломanganate
262 and not a tectomanganate such as todorokite. In contrast, subsurface and deeply buried
263 nodules are less affected by dehydration. The reflection shifts from ~ 9.7 Å to ~ 9.4 Å after
264 drying at 105°C and slightly decreases in intensity but there is not a simultaneous increase of
265 the ~ 7 Å reflection. This, together with the presence of two peaks at 2.45 Å and ~ 2.40 Å, is
266 indicative of the presence of todorokite (e.g., Manceau et al., 2014). The fact that the ~ 2.40 Å
267 peak is better defined in deeply buried nodules than in shallow buried nodules suggests an
268 increase in todorokite crystallinity or abundance with prevailing time under suboxic
269 conditions, sediment depth and (or) nodule ageing. Consistently, TEM micrographs (Fig.
270 6a,b) show the presence of tectomanganates intermixed with phylломanganates in dendritic
271 growth structures close to Fe-rich LGS (Fig. 6a,b) of a deeply buried nodule (22KL-801cm).
272 The tunnel sizes of the tectomanganates vary and are locally higher than the typical 3×3
273 octahedra of todorokite. Due to the varied tunnel sizes ($3 \times >3$) in this Mn mineral, it will be
274 referred to here as “defective todorokite” (Bodeř et al., 2011).

275

276 3.2.3 FTIR

277 FTIR spectra of surface and buried nodules are presented in Fig. 7. FTIR bands in the region
278 between 800 and 400 cm^{-1} are characteristic for Mn-O lattice vibrations (Kang et al., 2007).
279 Surface nodules have three FTIR bands around 430 (weak), ~ 466 (strong), and 512 - 526
280 (medium strong) cm^{-1} . Subsurface nodules also display a very weak shoulder around 430 cm^{-1} ,
281 and two medium strong peaks, in the range of 457 and 468 cm^{-1} and the other between 512
282 and 526 cm^{-1} . These three bands are in good agreement with the IR characteristics of layered
283 manganese oxides (Potter and Rossman, 1979; Golden et al., 1986; Kang et al., 2007).
284 Infrared bands of buried nodules are somewhat different between 500 and 400 cm^{-1} compared
285 to surface nodules and they have an additional band at ~ 760 cm^{-1} which is absent in nodules
286 from the sediment surface (Fig. 7). According to Julien et al. (2004) and Atkins et al. (2014)
287 the band at ~ 760 cm^{-1} is due to an asymmetrical Mn-O stretching vibration corresponding to
288 corner-sharing MnO_6 octahedra and is therefore characteristic for a tectomanganate structure
289 such as todorokite. Collectively, our data indicate that buried nodules contain
290 tectomanganates while surface nodules mainly contain phylломanganates.

291

292 3.3 EXAFS Results and Interpretation

293 3.3.1 Ni K-edge EXAFS

294 Ni *K*-edge EXAFS and the corresponding Fourier transforms (FT) are shown in Figure 8a and
295 8b and the modeling results are summarized in Table 1. All *k*-space data of surface and
296 subsurface nodules are similar. In contrast, those from deeply buried nodules, and especially
297 sample 22KL-801cm and 65SL-985cm, differ in the 6 - 7 Å⁻¹ region (Fig. 8a). According to
298 Manceau et al., 2007 the decrease in the oscillation of the Ni *K*-edge EXAFS in the region
299 between 6 and 7 Å⁻¹ is characteristic for higher amounts of Mn³⁺ in the octahedral sheets. This
300 matches our mineralogical data, which show that deeply buried nodules have todorokite as the
301 main mineral phase, which generally has a higher amount of Mn³⁺ in the structure than
302 phyllomanganates (e.g., Bodei et al., 2007).

303 The FT of all samples (surface, subsurface and buried nodules; Fig. 8b) have a peak at $R+\Delta R$
304 ≈ 1.6 Å corresponding to the first shell of O atoms around the absorbing atom (Ni-O; Peacock
305 and Sherman 2007a, b) that can be modeled with a shell of 6 O atoms at 2.01 – 2.05 Å (Table
306 1). The second peak (Ni-Mn) in the FT spectra of surface and subsurface nodules is located at
307 $R+\Delta R \approx 2.41 - 2.45$ Å (Fig. 8b). This peak was modeled with a shell of up to 6 Mn atoms at
308 2.84 – 2.87 Å (Table 1), typical for Ni structurally incorporated in the octahedral layers of
309 phyllomanganates (^ENi; Peacock and Sherman, 2007b; Manceau et al., 2014). A small peak is
310 also observed in the FT of Ni of surface nodules at $R+\Delta R \sim 3.1-3.2$ Å and could possibly be
311 attributed to Ni sorbed as a triple-corner (^TCNi) sharing complex over vacancies of
312 phyllomanganates or to Ni at the edges of the triple chains of a minor todorokite phase (e.g.,
313 Manceau et al., 2014; Bodei et al., 2007). However, attempts to quantify this component by
314 data modeling led to a proportion of 15 % of the total Ni in sample 44KG (Table 1), which is
315 within the typical uncertainty (~20 %) of EXAFS data analysis. Thus, in the following
316 discussion, we will make the assumption that Ni of surface and subsurface nodules from our
317 working area is mainly incorporated within the octahedral sheets of the phyllomanganates.

318 These results are in good agreement with previous Ni-EXAFS studies on phyllomanganates in
319 marine nodules and synthetic Ni-rich phyllomanganates such as birnessite (Peacock and
320 Sherman, 2007a, b; Manceau et al., 2007; Manceau et al., 2014; Atkins et al., 2016).

321 In buried nodules, the FT peak at $R+\Delta R \approx 2.39 - 2.45$ Å is less pronounced than in surface
322 nodules. Moreover, the peak intensity decreases with burial depth (subsurface to deeply
323 buried nodules; Fig. 8b). This suggests a decrease in the relative abundance of Ni
324 incorporated within the phyllomanganate sheets and/or lower amounts of neighbors around
325 the Ni atoms within the MnO₂ sheets. Data modeling of deeply buried nodules indicate that 35
326 – 76 % of Ni is incorporated in the phyllomanganate sheets (^ENi). The remaining fraction is
327 bound as a triple corner (^TCNi) complex over vacancies of phyllomanganates or is

328 incorporated within the edge of triple chains of todorokite, which is the main Mn-phase in
329 deeply buried nodules. In both cases the binding distances are expected to be 3.5 Å – 3.6 Å
330 (Peacock and Sherman 2007; Manceau et al., 2014). In our models, the modeled distance was
331 3.55 - 4.00 Å, but the number of neighbors was low (1 - 4; Table 1). In addition the FT data
332 do not show a distinct peak in this area (Fig. 8b).

333

334 **3.3.2 Cu *K*-edge EXAFS**

335 Cu *K*-edge EXAFS and the corresponding FT spectra are shown in Figure 9a and 9b.

336 The *k*-space data of surface, subsurface and deeply buried nodules (Fig. 9a) are significantly
337 different, with a resonance at $\sim 5.5 \text{ \AA}^{-1}$ that decreases in intensity with burial depth. The FT
338 spectra of all Cu *K*-edge EXAFS data have a peak at $R+\Delta R \sim 1.5 \text{ \AA}$ (Fig. 9b) that could be
339 modeled with 3 to 4 O atoms at 1.96 Å (Table 2), using the model proposed by Peña et al.
340 (2015). This implies that Cu is either in tetrahedral coordination or in octahedral-disordered
341 configuration (see discussions in Sherman and Peacock, 2010; Manceau et al., 2014). The
342 second distinct peak in the FT data, at $R+\Delta R \approx 2.45 \text{ \AA}$, corresponds to Cu-Mn distance, with a
343 modelled distance for ~ 2 atoms at 2.87 to 2.88 Å and 1 atom at 3.42 to 3.45 Å in surface
344 nodules (Table 2). These distances are compatible with Cu being incorporated at the edges of
345 the phylломanganate octahedra layers, within the plane formed by layer Mn (Peña et al.,
346 2015), and with Cu in a TC configuration, respectively. From the ratio of the number of Mn
347 atoms in each of these two shells, it is proposed that Cu incorporated in the layer is the main
348 species for all samples whose EXAFS spectrum was modelled.

349 Subsurface and deeply buried nodules display a decrease of the amplitude of the Cu-Mn peak
350 at $R+\Delta R \approx 2.45 \text{ \AA}$ with burial depth. The decreasing of the amplitude generally corresponds to
351 the decrease in the number of atomic neighbors, which is not clearly reflected in the data
352 modeling. However, it was observed that the modelled Debye-Waller factors of this path
353 increased, suggesting an increase in the degree of structural disorder in the Cu sites. However,
354 since these two parameters (number of atomic neighbors and structural disorder) are often
355 inversely correlated, this increase in structural disorder might also mask a decrease in the
356 mean number of Mn neighbors in each Cu-Mn shell. Modeling of the buried nodules with the
357 same structural model as the surface nodules was unsuccessful. Consequently, the Cu *K*-edge
358 EXAFS were not modeled for subsurface and deeply buried nodules, as the results were found
359 to be unreliable. However, the fact that the Cu *K*-edge EXAFS spectra of the buried nodules
360 have a shape close to a sinusoidal curve, suggests the presence of a single shell around Cu,
361 likely a Cu-O shell according to FT data (Fig. 9a).

362

363 **3.3.3 Cobalt *K*-edge EXAFS**

364 The mean Co *K*-edge EXAFS data of suboxic-diagenetic dendritic growth structures of a
365 deeply buried nodule (22KL-801 cm) and the associated FT spectra are presented in Figure
366 10a and 10b and the modeling fit is summarized in Table 3. Similar to Ni and Cu *K*-EXAFS
367 spectra, the Co *K*-EXAFS spectrum is composed of two main waves of differing frequencies
368 (Fig. 10a), as evidenced by the two main peaks in the FT (Fig. 10b). The first peak in Fig. 10b
369 corresponds to Co-O scattering ($R+\Delta R \approx 1.6 \text{ \AA}$) and the second peak to Co-Mn scattering
370 ($R+\Delta R \approx 2.44 \text{ \AA}$; Manceau et al., 2014; Wu et al., 2019).

371 Modeling of the data resulted in the best fits with two different Co-O distances of 1.94 \AA and
372 2.25 \AA (see Table 3). However, the second peak only forms a small shoulder in the FT
373 spectrum and is therefore only a minor component of the sample. The first distance is
374 characteristic for Co³⁺-O bonds and the second one is typical for Co²⁺-O pair (e.g., Manceau
375 et al., 1997). Furthermore, modelling of the first oxygen peak results in 6 oxygens, whereby
376 only 2.6 oxygen neighbors can be modeled for Co²⁺.

377 The second peak at $R+\Delta R=2.44 \text{ \AA}$ in FT (Fig. 10b) can be modeled with two Co-Mn bond
378 distances at 2.88 \AA and 3.08 \AA (Table 3). The first Co-Mn distance is typical for Co³⁺ being
379 incorporated within the octahedra sheets (^ECo), similar to Co incorporated in the octahedral
380 layers of phyllosulfates (Manceau et al., 1997; Manceau et al., 2014; Wu et al., 2019).
381 The second distance of 3.08 \AA cannot be clearly assigned.

382 In contrast to previous studies, where Co is mainly incorporated into the vernadite phase of
383 oxic-hydrogenetic LGS in surface nodules, Co in deeply buried nodules of this study is
384 incorporated into the Mn-phase of the suboxic-diagenetic LGS, which is a tectomanganate
385 such as todorokite according to the bulk XRD, IR measurements, and TEM analyses.

386

387 **4. DISCUSSION**

388 **4.1 Mineralogy of buried nodules: transformation of phyllosulfate to todorokite and** 389 **implications for the fate of metals**

390 Surface and buried nodules have distinctly different mineralogical compositions due to the
391 transformation of 10 \AA phyllosulfate into todorokite that can be related to the burial
392 process under oxic and suboxic conditions. Surface nodules are predominantly composed of
393 Fe-vernadite and of 7 \AA and 10 \AA vernadite having a hexagonal layer symmetry
394 (Wegorzewski and Kuhn, 2014; Wegorzewski et al., 2015). Todorokite is an accessory phase,

395 if present at all. In contrast, subsurface nodules (14-16 cm) are composed of both
396 phyllomanganates and defective todorokite, whereby the latter is certainly an intermediate
397 phase between phyllomanganate and tectomanganate (Bodeř et al., 2007). Nodules buried
398 deep in the sediments (>530 cm) have todorokite as the major Mn-oxide phase. Heller et al.,
399 (2018) showed that Mn-nodules buried in suboxic deep-sea sediments are subject to
400 diagenetic processes. These processes affect not only the chemical composition of the nodules
401 and the surrounding sediments (Heller et al., 2018) but also their mineralogy. However, the
402 exact transformation pathway from phyllomanganates to todorokite in the natural
403 environment is still unclear (e.g., Atkins et al., 2014; 2016).

404 The synthetic route in the laboratory to produce todorokite begins with a *c*-ordered Mg-rich
405 10 Å phyllomanganate, which is subsequently exposed to high temperatures to transform into
406 todorokite (~160°C; e.g., Bodeř et al., 2007). Different requirements are necessary for the
407 phyllomanganate-to-tectomanganate transformation: **(I)** stacking of several MnO₂ sheets, **(II)**
408 saturation of the interlayer with a cation capable of enforcing a ~10 Å layer-to-layer distance
409 (e.g., Mg²⁺) and **(III)** the presence of Jahn-Teller elements (e.g., Mn³⁺, Cu²⁺; Manceau et al.,
410 2014; Bodeř et al., 2007, Grangeon et al., 2014). If any of these requirements is not fulfilled,
411 the formation of tectomanganate from phyllomanganate is inhibited or incomplete (e.g., Bodeř
412 et al., 2007).

413 In general, nodules from the sediment surface of the study area have been exposed during
414 their growth history to alternately oxic and suboxic conditions (Wegorzewski and Kuhn,
415 2014; Kuhn et al., 2017b). As a result, hydrogenetic and suboxic-diagenetic LGS form.
416 During oxic conditions, hydrogenetic LGS are formed due to metal (e.g. Mn, Fe, Co)
417 precipitation from oxic seawater or oxic sediment pore water (Wegorzewski and Kuhn, 2014).
418 Those LGS consist of vernadite, which is epitaxially intergrown with amorphous Fe-
419 oxyhydroxides (δ -FeOOH) and has a Mn average oxidation state close to +4, which means
420 low amounts of layer and interlayer Mn³⁺. Moreover, vernadite contains a low amount of Cu²⁺
421 (0.34 ± 0.16 wt.%; Wegorzewski and Kuhn, 2014) and therefore in general low amounts of
422 Jahn-Teller elements (Mn³⁺, Cu²⁺). The Mg content of hydrogenetic LGS (0.3 – 3 wt.%) is
423 lower than of suboxic-diagenetic LGS (1-4 wt.%). Furthermore, the internal, older parts of the
424 surface nodules should predominantly consist of todorokite if this transformation would just
425 be kinetically-controlled. However, the internal older parts of these nodules have the same
426 alternating hydrogenetic and diagenetic LGS, as also observed in younger areas. According to

427 these results, we conclude that hydrogenetic vernadite is not able to transform to todorokite
428 via early diagenetic processes under oxic conditions.

429 In contrast, under suboxic conditions within the sediments, Mn^{4+} can be reduced to aqueous
430 Mn^{2+} that can be released into pore water and subsequently diffuses upward along
431 concentration gradients until it is re-oxidized at the site of Mn nodule formation, contributing
432 to diagenetic nodule growth. This process would lead to the formation of Mn-rich and Fe-poor
433 suboxic-diagenetic LGS.

434 The nodule dissolution under suboxic conditions can be accompanied by Mn^{2+} readsorption
435 by MnO_2 phases. In this case, Mn^{2+} will certainly react with Mn^{4+} to produce Mn^{3+} (Elzinga,
436 2016; Grangeon et al., 2017), leading to an increased Mn^{3+}/Mn^{4+} ratio in the remaining nodule
437 and thus favoring the phylломanganates to todorokite transformation.

438 Concomitant with the reduction of the Mn-phase, associated elements such as Ni, Cu, and Co
439 will be released in pore water where they will be available for incorporation in newly formed
440 suboxic-diagenetic phylломanganates having a Mn oxidation state lower than +4 and a Mg
441 content to 4 wt.% (Wegorzewski and Kuhn, 2014). The presence of a Jahn-Teller cation
442 (Mn^{3+}) and of an interlayer cation (Mg^{2+}) capable of enforcing a 10 Å layer-to-layer distance
443 suggests that phylломanganates of suboxic-diagenetic LGS have higher potential to transform
444 to todorokite during early diagenesis than vernadite of hydrogenetic LGS from the same
445 nodules. Therefore, we propose that if Mn-nodules become buried within suboxic sediments,
446 10 Å phylломanganates of suboxic-diagenetic LGS will preferentially transform to todorokite
447 over time. If nodules are exposed to suboxic conditions for a more extended period of time,
448 the mineralogical transformations will likely be accelerated or intensified and therefore the
449 crystal-chemistry of Ni, Cu and Co can be modified. More specifically, the hydrogenetic
450 vernadite will continue to dissolve under suboxic conditions and Mn^{2+} together with its
451 associated elements (Ni, Cu and especially Co) will be released into pore water (Manceau et
452 al., 2014). This hypothesis explains the observation of Heller et al. (2018), who showed that
453 deeply buried nodules have lower amounts of hydrogenetic LGS than surface nodules, and
454 also that Ni, Cu and Co are enriched in pore waters around buried nodules. Furthermore, it is
455 important to note that these buried nodules contain 40 % less Ni than nodules from the
456 sediment surface (Heller et al., 2018).

457 Our data support the idea that the formation of todorokite from a 10 Å phylломanganate
458 precursor in marine nodules is predominantly a solid-state transformation as Bodeř et al.
459 (2007) have proposed. As shown by Grangeon et al. (2014, 2015), Mn^{3+} located in the
460 octahedral sheets can spontaneously migrate to interlayer sites to minimize steric strains

461 (steric strain results from a mismatch between the ideal geometry of an ion coordination
462 sphere and the geometry of the crystallographic site of the ion) resulting from the Jahn-Teller
463 distortion of the octahedral sheets, and contribute to the building of the “walls” of
464 tectomanganates. The Jahn-Teller distortion is a geometric distortion of a nonlinear molecular
465 system, which reduces its symmetry and energy. In an octahedral complex, two axial bonds
466 are shorter/longer than the other four – (Chaudhary et al., 2015 and references therein). The
467 same process may also affect Cu^{2+} initially incorporated in the layers of phyllosulfates, as
468 well as the Mn^{3+} generated by interaction of the mineral surfaces with aqueous Mn^{2+} .
469 In contrast to our investigations, Elzinga (2011, 2016) showed that aqueous Mn^{2+} reacting
470 with hexagonal birnessite at pH 7.5 causes reductive transformation of birnessite into Mn^{3+} -
471 bearing Mn-phases such as feitknechite and manganite. If these Mn-phases are transformation
472 products, they should be present as minor phases in the studied nodules. However, we were
473 unable to detect these phases in our bulk XRD analyses. In our system, it is likely that the
474 ratio of Mn^{2+} in solution to phyllosulfates was lower than that required to produce
475 feitknechite or that the abundance of feitknechite was below 5% and as such was undetectable
476 by bulk XRD. However, we cannot strictly rule out that, despite all cautions taken for sample
477 preservation, traces of feitknechite were initially present in the samples and were oxidized by
478 atmospheric O_2 before sample analysis.

479

480 **4.2 Crystal chemistry of trace metals (Ni, Cu, Co) and their behavior during** 481 **mineralogical transformation**

482 Ni^{2+} and Cu^{2+} can be incorporated into phyllosulfates (I) by adsorption above or below
483 vacancy sites (forming a triple corner sharing complex: $^{\text{TC}}\text{Me}$, where Me is the cation of
484 interest), (II) by incorporation into a manganese layer sheet ($^{\text{E}}\text{Me}$), or (III) by adsorption at
485 lateral edge surfaces (e.g., double corner sharing: $^{\text{DC}}\text{Me}$; Manceau et al., 2014; Peacock et al.,
486 2007a, b; Peña et al., 2015). In contrast, Co generally occurs as Co^{3+} incorporated within the
487 octahedral sheets of phyllosulfates ($^{\text{E}}\text{Co}^{3+}$; Manceau et al., 2014).

488 The incorporation mechanism of these metals into tectomanganates such as todorokite is less
489 documented (Manceau et al., 2014; Atkins et al., 2016; Wu et al., 2019). Mn^{4+} occupies the
490 central and edge sites of the triple chains of todorokite tunnels while Mn^{3+} , Ni^{2+} and Cu^{2+}
491 exclusively occupy the edge sites (Post and Bish, 1988; Bodei et al., 2007, Manceau et al.,
492 2014). Furthermore, metals such as Ni^{2+} can also form an outer-sphere complex in the
493 todorokite tunnels (Pakarinen et al., 2010). To our knowledge, there are no data about the

494 location of Co into the todorokite structure of natural Mn-nodules. There are only few studies
495 in the laboratory about the transformation of Co-bearing phyllomanganates into
496 tectomanganates (Ching et al., 1999; Kumagai et al., 2005; Song et al., 2010; Wu et al., 2019).
497 Co is generally enriched during hydrogenetic growth and is therefore incorporated into
498 hydrogenetic vernadite rather than into suboxic-diagenetic Mn oxides.
499 In the following sections we will discuss the incorporation mechanism of Ni, Cu and Co in
500 Mn-phases of deeply buried nodules in contrast to nodules from the sediment surface.

501

502 **4.2.1 Nickel**

503 Ni in surface nodules from this study is incorporated within the octahedra of the
504 phyllomanganate sheets (^ENi; Fig. 8b; Fig. 11a,b). In contrast, in deeply buried nodules
505 (530cm – 987cm), Ni is mostly bound to todorokite. We propose that Ni preferentially
506 occupies the middle sites of the triple octahedra chains (^ENi) or the sites at the edges of the
507 triple chains (^{TC}Ni; minor amount, Fig. 12a,b). With our assumption, Ni in todorokite of
508 buried nodules can be expected to have fewer neighbors in the middle of the three octahedra
509 than in phyllomanganates of surface nodules. This would explain the decrease of the $R+\Delta R \approx$
510 2.39 \AA peak amplitude and furthermore the absence of a distinct peak at $R+\Delta R \approx 3.2 \text{ \AA}$ in the
511 FT Ni-EXAFS spectra (Fig. 8b). However, an alternative explanation for the decrease of the
512 ^ENi peak at $R+\Delta R \approx 2.39 \text{ \AA}$ and the absence of a distinct peak for Ni in the octahedra triple
513 chains of todorokite would be that Ni could be present in a disordered environment or that a
514 part of the Ni forms an outer-sphere complex in the tunnels of todorokite (Fig. 12b; Pakarinen
515 et al., 2010). Atkins et al., (2016) showed that during the transformation of a synthetic Ni-
516 bearing phyllomanganate into todorokite, up to 50 % of the Ni was released, which is similar
517 to what we observe here. As noted above in section 4.1, nodules from the sediment surface
518 consist of phyllomanganates and contain 40 % more Ni than the deeply buried nodules, which
519 consist mainly of todorokite (Wegorzewski and Kuhn, 2014; Wegorzewski et al., 2015; Heller
520 et al., 2018). Furthermore, sample 22KL-801cm shows a modeled Ni-Mn distance of 4, which
521 cannot be attributed to ^ENi incorporation in phyllomanganates or todorokite. Our Ni-EXAFS
522 analysis of buried nodules indicates that Ni is released in solution during the
523 phyllomanganate-to-tectomanganate transformation.

524

525 **4.2.2 Copper**

526 According to Heller et al. (2018), Cu concentration in nodules from the sediment surface and
527 those buried are similar. In contrast to Ni²⁺, Cu²⁺ favors the transformation from

528 phylломanganates into tectomanganates and may remain in the structure during this
529 transformation (Burns and Burns 1978; Usui, 1979; Atkins et al., 2016).

530 Modeling Cu-EXAFS of surface nodules with the model of Peña et al. (2015) shows that Cu
531 is preferentially incorporated as ^ECu , similar to Ni, but with fewer atomic neighbors resulting
532 in a lower amplitude of the $^E\text{Cu-Mn}$ peak compared to the $^E\text{Ni-Mn}$ peak (Fig. 11a). These
533 results may be interpreted in terms of the Cu in surface nodules being preferentially located at
534 the edges of the phylломanganate sheets with only 3 to 4 atomic neighbors (Fig. 11b; Peña et
535 al., 2015). In all nodules, ^{TC}Cu is present in low amounts, as witnessed by the low intensity of
536 the correlation at $R+\Delta R \approx 3.2 \text{ \AA}$ in the FT and by data modeling (Fig. 9b, 11a; Table 2).

537 In contrast to surface nodules, Cu-EXAFS data of the deeply buried nodules show a
538 sinusoidal curve in the k -space, which suggests only one coordination shell (Fig. 9a). The FT
539 data of these Cu-EXAFS data have only one distinct peak around $R+\Delta R \approx 1.5 \text{ \AA}$ suggesting
540 that O is the only neighbor of Cu compared to FT Ni-EXAFS data of deeply buried nodules
541 (Fig. 8; 12). These results suggest that Cu is bound as an outer-sphere complex in todorokite
542 of deeply buried nodules (Fig. 12b), as previously assumed for Ni (Pakarinen et al., 2010).

543 Another explanation could be that Cu is increasingly bound in a disordered configuration to
544 one or more sorption site(s) with increasing depth of burial.

545 Furthermore, we compared the Cu-EXAFS data of bulk nodules of this study with Cu-EXAFS
546 analyses of Manceau et al. (2014) (Fig. 13). The authors recorded Cu-EXAFS of a
547 phylломanganate-rich area, a todorokite-rich area, and a clay-rich area in a natural Mn nodule
548 from the Pacific Ocean. The Cu-EXAFS of surface nodules from this study
549 (phylломanganate-rich) are similar to Cu-EXAFS of the todorokite-rich region (CuD465D2)
550 of Manceau et al. (2014). In contrast, Cu-EXAFS analyses of subsurface nodules of this study
551 (phylломanganates and todorokite/defective todorokite) match well with Cu-EXAFS of the
552 phylломanganate-rich region of the surface nodule (CuD465D1; Manceau et al., 2014; Fig.
553 13).

554 One could expect that, as nodules from the sediment surface become buried and thus as
555 phylломanganates transform to todorokite, Cu remains in the crystal structure of the Mn
556 oxides. This would produce a spectrum for buried nodules that would be close to that reported
557 by Manceau et al. (2014; CuD465D2), with a dominant peak at 3.5 \AA , which is not the case
558 (Fig. 9a, b). We speculate that Cu underwent an additional step with regards to the
559 aforementioned mechanisms; after it Cu was incorporated within the Mn sites at the edges of
560 the triple chains of todorokite (Post and Bish, 1988; Post et al., 2003; Bodai et al., 2007;
561 Manceau et al., 2014), but subsequently migrated out of the structure after the nodules were

562 subject to suboxic conditions for a longer period of time (Fig. 12b). If nodules become
563 exposed to suboxic conditions for a long period of time, not only vernadite of hydrogenetic
564 LGS dissolves, but the 7 Å and 10 Å phyllomanganates as well as todorokite will also begin
565 to dissolve. In the course of the Mn dissolution, Cu will be released from Mn octahedra,
566 migrate into the tunnels or at the todorokite surface, or adsorb to another phase, and would in
567 all cases form an outer-sphere complex before being ultimately released into the pore water.
568 Coherently, the Cu-EXAFS spectrum of deeply buried Mn-nodules agrees well with that of
569 clay-rich regions (smectite-rich; CuD465DH; Manceau et al., 2014, Fig. 13a,b). According to
570 a number of authors (Boström et al., 1974; Manceau et al., 2014), Cu may also be associated
571 with organic matter, biogenic silica, phosphates, carbonates or aluminosilicates that may also
572 show FT data of Cu-EXAFS with sinusoidal curves and only one distinct peak around
573 $R+\Delta R \sim 1.5$ Å. However, our statistical analyses, individual high resolution measurements
574 using electron microprobe, as well as leaching experiments of surface and buried nodules, all
575 suggest that Cu is strongly associated with Mn oxides and to a lesser degree with Fe
576 oxyhydroxides and not with other phases in the Mn-nodules (e.g., Mohwinkel et al., 2014;
577 Wegorzewski and Kuhn, 2014; Heller et al., 2018). Further work would be required to explain
578 this potential discrepancy, and discriminate between a difference in sorption site and in an
579 intimate association of different minerals (e.g., Mn oxides and a minor amount of clays) that
580 would thus be hardly distinguishable with the method used here. Note however that the
581 presence of Cu bound to organic matter is unlikely, as the total organic carbon content of the
582 present samples is $\leq 0.05\%$.

583

584 **4.2.3 Cobalt**

585 The enrichment of Co in the suboxic-diagenetic LGS of Mn-nodules from the CCZ is unusual
586 because Co is typically enriched in oxic-hydrogenetic vernadite due to oxidative scavenging
587 on Mn-oxides (Kuhn et al., 2017a), following well documented mechanisms (e.g., Koschinsky
588 and Halbach, 1995; Byrne, 2002; Manceau et al., 1997; 2014).

589 Our Co *K*-EXAFS analyses show that Co is predominantly incorporated as ${}^E\text{Co}^{3+}$ in the
590 phyllomanganates while, in the case of todorokite, it would be incorporated at a Mn site
591 located in the Mn row that is not adjacent to a “wall”, because no correlation ~ 3.4 Å
592 (Manceau et al., 1997; Fig. 12b) could be observed in the FT. Our Co-EXAFS data are similar
593 to those from a hydrogenetic area (D465H) in a nodule examined by Manceau et al. (2014) in
594 which all Co is incorporated into vernadite. According to our EPMA maps of the buried

595 nodule, Co is highly enriched (1.2 wt.%; Heller et al., 2018) in the suboxic-diagenetic
596 dendritic LGS, which are made up of “defective todorokite”/todorokite instead of vernadite.
597 Based on the presence of a second Co-O distance, a small proportion of Co occurs as Co^{2+} .
598 The modeled Co-Mn distance of 3.08 Å was attributed to this Co^{2+} , since it is too short for
599 Co^{3+} sharing corners with Mn octahedral in todorokite, or for surface adsorption of Co at
600 triple corner and/or edge sites on layered Mn oxides (^{57}Co ; Manceau et al., 1997; Wu et al.,
601 2019).

602 Asbolane was not detected in the bulk analysis of deeply buried nodules; therefore we
603 speculate that CoOOH is not present in our samples.

604 However, the high enrichment of Co in suboxic-diagenetic LGS is uncommon and may be
605 explained by secondary enrichment processes. Over time, as buried Mn-nodules become
606 exposed to suboxic environmental conditions, vernadite of hydrogenetic LGS starts to
607 dissolve, whereas the 10 Å phyllosulfates of diagenetic LGS remain stable. During
608 dissolution of vernadite the Mn-associated elements Ni, Cu, and especially Co will be
609 released into pore water (as Co^{2+}) and are available for further re-incorporation into the more
610 stable Mn-phases such as 10 Å phyllosulfates or newly formed todorokite. It is interesting
611 to note that only Co is significantly enriched in those phases and not Ni or Cu. A possible
612 mechanism might be a redox coupling of dissolved Co^{2+} with solid-phase Mn^{4+} , where Co^{2+} is
613 oxidized to Co^{3+} and Mn^{4+} is reduced to soluble Mn^{2+} (Heller et al., 2018). The similar ionic
614 radius of Co^{3+} and Mn^{4+} (0.53 Å versus 0.54 Å) allows Co^{3+} to substitute for Mn^{4+} in the
615 middle of the octahedral chains of todorokite after the transformation of phyllosulfates to
616 todorokite (Fig. 12).

617 The occurrence of minor amounts of Co^{2+} in the deeply buried nodules can arise from: (i)
618 Co^{2+} that remains adsorbed at edges of the Mn octahedra sheets or (ii) Co^{2+} -hydroxides that
619 form in the interlayer of defective todorokite structures (cf asbolane); or (iii) Co^{2+} formed by
620 reduction of Co^{3+} recently released from dissolving Mn-phases (together with Ni and Cu).
621 The latter hypothesis is supported by an increase of Co^{2+} concentration in pore water in the
622 sediment depth around the deeply buried nodules (Heller et al., 2018).

623

624 **4.3 Location of nodule formation**

625 In the discussion provided above we suggest that all buried nodules of this study primarily
626 formed at the sediment surface and were subsequently buried within the sediment column. We
627 do not think that the buried nodules were formed in situ within the sediments as a sedimentary
628 layer.

629 This is because: (1) The shape and morphology, as well as the internal growth structures
630 (hydrogenetic and suboxic-diagenetic LGS), are very similar to surface nodules (Halbach et
631 al., 1988; Wegorzewski and Kuhn, 2014). (2) The buried nodules clearly show signs of
632 dissolution such as a grainy surface, brittle appearance and dissolved internal layers (Heller et
633 al., 2018). (3) Diagenetic Mn-oxide formation in deep sea sediments would form continuous
634 layers rather than single, individual nodules (Thomson et al., 1987; Jarvis and Higgs, 1987).
635 (4) In this area, Mn-nodules can become buried within the sediment due to increased
636 sedimentation rates (von Stackelberg 1997). (5) In general the formation of all Mn-nodules
637 needs the presence of an oxic/suboxic front at the position of nodule formation. Only the
638 sediment surface provides stable conditions over a long period of time for the presence of
639 such a front. In contrast, within the sediments the location of this front moves up and down
640 due to varying sedimentation conditions (sedimentation rates, flux of organic material). (6)
641 The current oxic/suboxic front within the sediment column of the working area is located at 2-
642 3 m sediment depth (Mewes et al., 2014). We have not found Mn-nodules at this front in any
643 of these cores (Kuhn et al., 2015; Heller et al., 2018; Mewes et al., 2014). Mn-nodules were
644 either found below or above this front.

645

646 **5. SUMMARY AND CONCLUSIONS**

647 This study identifies the processes that occur during mineral transformation of Mn oxide
648 phases of Mn-nodules under suboxic conditions in the deep-sea sedimentary environment, and
649 how those transformations influence the distribution of Ni, Cu, and Co. Mn-nodules from the
650 sediment surface are typically mixed-type nodules consisting of hydrogenetic and suboxic-
651 diagenetic LGS. Hydrogenetic LGS consist of vernadite and amorphous FeOOH, and the
652 suboxic-diagenetic LGS consist of 7 Å and 10 Å phyllomanganates. From EXAFS data, Ni in
653 surface nodules is incorporated at random sites of the manganese layer sheets with up to 6
654 atomic neighbors, whereas Cu is preferentially incorporated at the edges of the
655 phyllomanganate sheets with lower amount of atomic neighbors.

656 In subsurface nodules, phyllomanganates start to transform to tectomanganates, but Cu, Ni
657 and Co remain incorporated within the octahedral Mn oxide sheets.

658 In contrast, the deeply buried nodules (>530 cm) predominantly consist of tectomanganates
659 such as todorokite. Nickel in deeply buried nodules is primarily incorporated as ^ENi in the
660 middle of the octahedra chains forming the todorokite tunnels and probably partly being
661 bound as outer-sphere complexes within the todorokite tunnels. In contrast, Cu in deeply
662 buried nodules appears to be completely bound as outer-sphere complexes within the

663 todorokite tunnels. Like Ni, Co appears to be incorporated mainly in the middle of octahedral
664 chains of todorokite in deeply buried nodules.

665 In general, all of the Mn-nodules, independent of their location in the sediment column, are or
666 were mixed type nodules consisting of hydrogenetic as well as suboxic-diagenetic LGS.
667 Subsurface and deeply buried nodules likely formed at the sediment surface, and were
668 subsequently buried due to a change in sedimentation rate or other geological events. Since
669 sub-surface nodules are older than surface nodules (unpublished BGR data), they have been
670 subject to suboxic diagenetic processes over a longer period of time which may have
671 promoted the transformation of phylломanganates to tectomanganates.

672 However, if mixed type nodules are buried at depth with prolonged suboxic conditions, then
673 Mn oxide phases start to dissolve. At the beginning of the dissolution only vernadite of
674 hydrogenetic LGS dissolve, releasing Mn^{2+} and associated metals such as Co^{2+} into pore
675 waters. Dissolved Mn^{2+} can react with the more stable 7 Å and 10 Å phylломanganates and
676 transforms them into tectomanganates such as todorokite. Furthermore, the released Co^{2+} can
677 be re-adsorbed on the more stable Mn oxide phase (in this case “defective
678 todorokite”/todorokite) and will be incorporated into the octahedral structure of the
679 tectomanganates due to a redox-reaction with Mn^{4+} and/or Mn^{3+} . If these nodules remain
680 under such suboxic conditions, the more ordered Mn-phases such as todorokite will also start
681 to dissolve and only the Fe-phases (δ -FeOOH/ Fe_2O_3) will eventually remain. Furthermore,
682 during the Mn-oxide dissolution, Ni and Cu start to migrate from the octahedra sheets into the
683 tunnels or above the sheets and will be adsorbed as outer-sphere complexes before being
684 completely released into the sediment pore waters.

685

686 **ACKNOWLEDGEMENTS**

687 We greatly appreciate the work of the master and his crew on expeditions SO205 and SO240
688 with R/V Sonne during which the samples for this study were taken.

689 We thank C. Wöhrl and S. Goldmann for an excellent support during the EMP analysis at the
690 Federal Institute for Geosciences and Natural Resources (BGR). We also thank M. Hein
691 (BGR) for conducting the IR-spectroscopy and S. Kaufhold (BGR) for discussing the IR
692 results. Furthermore, we gratefully acknowledge the expert help of Mrs. A. Schreiber from the
693 GFZ in Potsdam for foil preparation using FIB and Dr. Fabienne Warmont for the HRTEM
694 analyses. This work was funded as internal BGR project (Project: MeMa: A-0203008.A) and
695 by the German Federal Ministry for Education and Research (BMBF) under the grant
696 03G0240A. S. Grangeon acknowledges funding by the French National Research Agency

697 (ANR, grant ANR-14-CE01-0006) and by a BRGM project. Furthermore, we gratefully thank
698 the beam line scientist R. Davis (beam line 4-1) at the SSRL for helping during the EXAFS
699 measurements. Use of the Stanford Synchrotron Radiation Lightsource, SLAC National
700 Accelerator Laboratory, is supported by the U.S. Department of Energy, Office of Science,
701 and Office of Basic Energy Sciences under Contract No. DE-AC02-76SF00515. The SSRL
702 Structural Molecular Biology Program is supported by the DOE Office of Biological and
703 Environmental Research, and by the National Institutes of Health, National Institute of
704 General Medical Sciences (including P41GM103393). The contents of this publication are
705 solely the responsibility of the authors and do not necessarily represent the official views of
706 NIGMS or NIH.

707

708 REFERENCES

709 Atkins, A.L., Shaw, S. and Peacock, C.L. (2014) Nucleation and growth of todorokite from
710 birnessite: Implications for trace-metal cycling in marine sediments. *Geochim. Cosmochim.*
711 *Acta* **144**, 109-125.

712 Atkins, A.L., Shaw, S. and Peacock, C.L. (2016) Release of Ni from birnessite during
713 transformation of birnessite to todorokite: Implications for Ni cycling in marine sediments.
714 *Geochim. Cosmochim. Acta* **189**, 158 – 183.

715 Banerjee, R., Iyer, S.D. and Dutta, P. (1991) Buried nodules and associated sediments from
716 the Central Indian Basin. *Geo-Mar Lett* **11**, 103-107.

717 Blöthe, M., Wegorzewski, A.V., Müller, C., Simon, F., Kuhn, T. and Schippers, A. (2015)
718 Manganese-Cycling Microbial Communities Inside Deep-Sea Manganese Nodules. *Environ.*
719 *Sci. Technol.* **49**, 7692-7700.

720 Bodeï, S., Manceau, A., Geoffroy, N., Baronnet, A., Buatier, M. (2007) Formation of
721 todorokite from vernadite in Ni-rich hemipelagic sediments. *Geochim. Cosmochim. Acta* **71**,
722 5698–5716.

723 Boström, K., Joensuu, O. and Brohm, I. (1974) Plankton: Its chemical composition and its
724 significance as a source of pelagic sediments. *Chem. Geol.* **14**, 255–271.

725 Burns R.G. and Burns V.M. (1977) Mineralogy of ferromanganese nodules. *Marine*
726 *Manganese Deposits* (ed. G.P. Glasby). Elsevier, Amsterdam.

727 Burns, V.M. and Burns, R.G. (1978) Authigenic todorokite and phillipsite inside deep-sea
728 manganese nodules. *Am. Mineral.* **63**, 827–831.

729 Byrne R.H., (2002). Inorganic speciation of dissolved elements in seawater: the influence of
730 pH on concentration ratios. *Geochem. Trans.*, **2**, 11-16.

731 Chaudhary, T., Khamar, J., Chaudhary, P., Chaudhary, V., Barot, M., & Sen, D. J. (2015).
732 Jahn–Teller distortions: a new strategy in quantum mechanics. *J Drug Discov Therap.* **3**, 09-
733 16.

734 Ching, S., Krukowska, K.S. and Suib, S.L. (1999). A new synthetic route to todorokite-type
735 manganese oxides. *Inorg. Chim. Acta* **294**, 123-132.

736 Cronan, D.S. and Tooms, J.S. (1967) Sub-surface concentrations of manganese nodules in
737 Pacific sediments. *Deep Sea Res.* **14**, 117-119.

738 Davison, W. (1993) Iron and manganese in lakes. *Earth-Sci. Rev* **34**, 119-163.

739 Drits, V.A., Silvester, E., Gorshkov, A.I. and Manceau, A. (1997) Structure of synthetic
740 monoclinic Na-rich birnessite and hexagonal birnessite: I. Results from X-ray diffraction and
741 selected-area electron diffraction, *Am. Mineral.* **82**, 946–961.

742 Drits, V.A., Lanson, B. and Gaillot, A.C. (2007). Birnessite polytype systematics and
743 identification by powder X-ray diffraction. *Am. Mineral.*, **92**, 771-788.

744 Elzinga, E.J. (2011). Reductive transformation of birnessite by aqueous Mn (II). *Environ. Sci.*
745 *Technol.* **45**, 6366-6372.

746 Elzinga, E. J. (2016). ⁵⁴Mn radiotracers demonstrate continuous dissolution and
747 reprecipitation of vernadite (δ -MnO₂) during interaction with aqueous Mn (II). *Environ. Sci.*
748 *Technol.* **50**, 8670-8677.

749 Giannuzzi, L.A., and Stevie, F.A. (2005) Introduction to Focused Ion Beams: Instrumentation,
750 Theory, Techniques and Practice, 98 p. Springer, Berlin.

751 Giannuzzi, L.A., Drown, J.L., Brown, S.R., Irwin, R.B. and Stevie, F.A. (1997) Focused ion
752 beam milling and micromanipulation lift-out for site-specific cross-section TEM specimen
753 preparation. In R. Anderson and S. Walck, Eds., Proceedings of the Materials Research
754 Society: Workshop on Specimen Preparation for TEM of Materials IV, 480. Materials
755 Research Society, Pittsburgh, Pennsylvania, p. 19–27.

756 Golden, D.C., Dixon, J.B. and Chen, C.C. (1986) Ion exchange, thermal transformations, and
757 oxidizing properties of birnessite. *Clays Clay Miner.* **34**, 511–520.

758 Grangeon, S., Fernandez-Martinez, A., Warmont, F., Gloter, A., Marty, N., Poulain, A. and
759 Lanson, B. (2015). Cryptomelane formation from nanocrystalline vernadite precursor: a high
760 energy X-ray scattering and transmission electron microscopy perspective on reaction
761 mechanisms. *Geoch. Trans.*, **16**, 12.

762 Grangeon, S., Lanson, B. and Lanson, M. (2014) Solid-state transformation of nanocrystalline
763 phyllomanganate into tectomanganate: influence of initial layer and interlayer structure. *Acta*
764 *Crystallographica Section B: Structural Science, Cryst. Res. Technol.* **70**, 828-838.

765 Grangeon, S., Warmont, F., Tournassat, C., Lanson, B., Lanson, M., Elkaïm, E. and Claret, F.
766 (2017). Nucleation and growth of feitknechtite from nanocrystalline vernadite precursor. *Eur J*
767 *Mineral*, **29**, 767-776.

768 Halbach, P., Friedrich, G., von Stackelberg, U., 1988. The Manganese Nodule Belt of the
769 Pacific Ocean. Geological Environment, Nodule Formation, and Mining Aspects. Ferdinand
770 Enke Verlag, Stuttgart, pp. 254

771 Haeckel, M., König, I., Riech, V., Weber, M. E. and Suess, E. (2001). Pore water profiles and
772 numerical modelling of biogeochemical processes in Peru Basin deep-sea sediments. *Deep*
773 *Sea Research Part II: Topical Studies in Oceanography*, **48**, 3713-3736.

774 Hein, J.R., Mizell, K., Koschinsky, A. and Conrad, T.A. (2013) Deep-ocean mineral deposits
775 as a source of critical metals for high- and green-technology applications: Comparisons with
776 land-based resources. *Ore Geol. Rev.* **51**, 1-14.

777 Heller, C., Kuhn, T., Versteegh, G.J.M., Wegorzewski, A.V., and Kasten, S. (2018). The
778 geochemical behavior of metals during alteration of manganese nodules buried in deep-sea
779 sediments. *Deep Sea Res. Part I: Oceanographic Research Papers*,

780 Heye, D., Marchig, V. and Meyer, H. (1979). The growth of burial manganese nodules. *Deep*
781 *Sea Res.* **26A**, 789-798.

782 Jarvis, I., Higgs, N. (1987): Trace-element mobility during early diagenesis in distal
783 turbidites: late Quaternary of the Madeira Abyssal Plain, N Atlantic. In: P.P.E. Weaver, J.
784 Thompson (eds). *Geology and Geochemistry of Abyssal Plains*. Geological Society Special
785 *Publications* **31**, pp. 179-213.

786 Julien, C. M., Massot, M. and Poinignon, C. (2004) Lattice vibrations of manganese oxides:
787 Part I. Periodic structures. *Spectrochim. Acta A: Molecular and Biomolecular Spectroscopy*
788 **60**, 689-700.

789 Kang, L., Zhang, M., Liu, Z. H., and Ooi, K. (2007). IR spectra of manganese oxides with
790 either layered or tunnel structures. *Spectrochim. Acta A: Molecular and Biomolecular*
791 *Spectroscopy* **67**, 864-869.

792 Koschinsky, A. and Halbach, P. (1995) Sequential leaching of marine ferromanganese
793 precipitates: genetic implications. *Geochim. Cosmochim. Acta* **59**, 5113–5132.

794 Koschinsky, A. and Hein, J. R. (2003). Uptake of elements from seawater by ferromanganese
795 crusts: solid-phase associations and seawater speciation. *Mar. Geol.*, **198**, 331-351.

796 Koschinsky, A., and Hein, J. R. (2017). Marine ferromanganese encrustations: Archives of
797 changing oceans. *Elements: An International Magazine of Mineralogy, Geochemistry, and*
798 *Petrology*, **13**, 177-182.

799 Kuhn, T. and Shipboard Scientific Party (2015) Low-temperature fluid circulation at
800 seamounts and hydrothermal pits: Heat flow regime, impact on biogeochemical processes and
801 its potential influence on the occurrence and composition of manganese nodules in the NE
802 Pacific, Cruise Report SO240/FLUM: Hannover, Germany, 185 p.

803 Kuhn, T., Wegorzewski, A., Rühlemann, C., Vink, A. (2017a) Composition, formation, and
804 occurrence of polymetallic nodules. In: Sharma, R., (eds.). *Deep-Sea Mining*. Springer,
805 Cham, pp. 23-63.

806 Kuhn, T., Versteegh, G.J.M., Villinger, H., Dohrmann, I., Heller, C., Koschinsky, A., Kaul,
807 N., Ritter, S., Wegorzewski, A.V. and Kasten, S. (2017b) Widespread seawater circulation in
808 18–22 Ma oceanic crust: Impact on heat flow and sediment geochemistry. *Geol.* **45**, 799-802.

809 Kumagai, N., Komaba S., Abe, K. and Yashiro, H. (2005). Synthesis of metal-doped
810 todorokite-type MnO₂ and its cathode characteristics for rechargeable lithium batteries. *J.*
811 *Power Sources* **146**, 310-314.

812 Lynn, D. C. and Bonatti, E. (1965) Mobility of manganese in diagenesis of deep-sea
813 sediments. *Mar. Geol.* **3**, 457-474.

814 Manceau, A., Lanson, M. and Geoffroy, N. (2007) Natural speciation of Ni, Zn, Ba and As in
815 ferromanganese coatings on quartz using X-ray fluorescence, absorption and diffraction.
816 *Geochim. Cosmochim. Acta* **71**, 95–128.

817 Manceau, A., Lanson, M. and Takahashi, Y. (2014) Mineralogy and crystal chemistry of Mn,
818 Fe, Co, Ni, and Cu in a deep-sea Pacific polymetallic nodule. *Am. Mineral.* **99**, 2068-2083.

819 Manceau, A., Drits, V.A., Silvester, E., Bartoli, C., and Lanson, B. (1997) Structural
820 mechanism of Co²⁺ oxidation by the phylломanganate buserite. *Am. Mineral.*, **82**, 1150–1175.

821 Moore, W.S. (1981) Iron-manganese banding in Oneida Lake ferromanganese nodules. *Nat.*
822 **292**, 233-235.

823 Mohwinkel, D., Kleint, C. and Koschinsky, A. (2014). Phase associations and potential
824 selective extraction methods for selected high-tech metals from ferromanganese nodules and
825 crusts with siderophores. *Appl. Geochem.* **43**, 13-21.

826 Pakarinen, J., Koivula, R., Laatikainen, M., Laatikainen, K., Paatero, E. and Harjula, R.
827 (2010) Nanoporous manganese oxides as environmental protective materials—Effect of Ca
828 and Mg on metals sorption. *J. Hazard. Mater.* **180**, 234-240.

829 Pal’chik, N.A., Grigor’eva, T.N. and Moroz, T.N. (2011) Natural and synthetic manganese
830 minerals. *Russ. J. Inorg. Chem.* **58**, 138–143.

831 Pattan, J.N. and Parthiban, G. (2007). Do manganese nodules grow or dissolve after burial?
832 Results from the Central Indian Ocean Basin. *J. Asian Earth Sci.* **30**, 696-705.

833 Peacock, C.L. (2009): Physiochemical controls on the crystal-chemistry of Ni in birnessite:
834 Genetic implications for ferromanganese precipitates. *Geochim. Cosmochim. Acta* **73**, 3568 –
835 3578.

836 Peacock, C.L. and Sherman, D.M. (2007a) Sorption of Ni by birnessite: Equilibrium controls
837 on Ni in seawater. *Chem. Geol.* **238**, 94 – 106.

838 Peacock, C.L. and Sherman, D.M. (2007b) Crystal-chemistry of Ni in marine ferromanganese
839 crusts and nodules. *Am. Mineral.* **92**, 1087 – 1092.

840 Peña, J., Bargar, J. R. and Sposito, G. (2015). Copper sorption by the edge surfaces of
841 synthetic birnessite nanoparticles. *Chem. Geol.* **396**, 196-207.

842 Potter, R.M. and Rossman, G.R. (1979) The tetravalent manganese oxides: identification,
843 hydration, and structural relationships by infrared spectroscopy. *Am. Mineral.* **64**, 1199-1218.

844 Post, J.E. and Bish, D.L. (1988) Rietveld refinement of the todorokite structure. *Am. Mineral.*
845 **73**, 861–869.

846 Ravel, B. and Newville M. (2005) ATHENA, ARTEMIS, HEPHAESTUS: data analysis for
847 X-ray absorption spectroscopy using IFEFFIT. *J SYNCHROTRON RADIAT* **4**, 537-541.

848 Rühlemann, C., Kuhn, T., Wiedicke, M., Kasten, S., Mewes, K. and Picard, A. (2011) Current
849 status of manganese nodule exploration in the German license area. In Ninth ISOPE Ocean
850 Mining Symposium. International Society of Offshore and Polar Engineers.

851 Rühlemann, C. and Shipboard Scientific Party (2018). MANGAN 2018 Cruise Report:
852 Geology, Biodiversity and Environment of the German License Area for the Exploration of
853 Polymetallic Nodules in the Equatorial NE Pacific, Guayaquil, Ecuador – Suva, Fiji, 6th April
854 – 29th May 2018, February 2019, Bundesanstalt für Geowissenschaften und Rohstoffe
855 (BGR), Hannover, Germany.

856 Sherman, D.M. and Peacock, C.L. (2010) Surface complexation of Cu on birnessite (δ -
857 MnO_2): Controls on Cu in the deep ocean. *Geochim. et Cosmochim. Acta* **74**, 6721 – 6730.

858 Song, C., Li, R., Liu, F., Feng, X., Tan, W. and Qiu, G. (2010). Cobalt-doped todorokites
859 prepared by refluxing at atmospheric pressure as cathode materials for Li batteries.
860 *Electrochim. Acta* **55**, 9157-9165.

861 Tazaki, K. (2000). Formation of banded iron-manganese structures by natural microbial
862 communities. *Clays Clay Miner.* **48**, 511-520.

863 Thomson, J., Colley, S., Higgs, N.C., Hydes, D.J., Wilson, T.R.S., Sorensen, J. (1987).
864 Geochemical oxidation fronts in NE Atlantic distal turbidites and their effects in the
865 sedimentary record. In: P.P.E. Weaver, J. Thompson (eds). *Geology and Geochemistry of*
866 *Abyssal Plains*. Geological Society Special Publications 31, pp. 167-177.

867 Uspenskaya, T.Y., Gorshkov, A.I. and Sivtsov, A.V. (1987) Mineralogy and internal structure
868 of Fe-Mn-nodules from the Clarion-Clipperton fracture zone. *Int. Geol. Rev.* **29**, 363–371.

869 Usui, A., and Terashima, S. (1997). Deposition of hydrogenetic and hydrothermal manganese
870 minerals in the Ogasawara (Bonin) arc area, northwest Pacific. *Mar. Geores. and Geotech.* **15**,
871 127-154.

872 Usui, A. (1979) Minerals, metal contents, and mechanism of formation of manganese nodules
873 from the central Pacific basin (GH76-1 and GH77-1 Areas). *Mar. Geol. Oceanography of the*
874 *Pacific manganese nodule province*, pp.651-679.

875 Villalobos, M., Toner, B., Bargar, J., and Sposito, G. (2003) Characterization of the
876 manganese oxide produced by *Pseudomonas putida* strain MnB1. *Geochim. Cosmochim. Acta*
877 **67**, 2649–2662.

878 Von Stackelberg, U., (1997) Growth history of manganese nodules and crusts of the Peru
879 Basin. Geological Society, London, Special Publications, 119, pp.153-176.

880 Wegorzewski, A.V. and Kuhn, T. (2014) The influence of suboxic diagenesis on the
881 formation of manganese nodules in the Clarion Clipperton nodule belt of the Pacific Ocean.
882 *Mar. Geol.* **357**, 123-138.

883 Wegorzewski, A.V., Kuhn, T., Dohrmann, R., Wirth, R. and Grangeon S. (2015)
884 Mineralogical characterization of individual growth structures of Mn-Nodules with different
885 Ni+Cu content from central Pacific Ocean. *Am. Mineral.* **100**, 2497-2508.

886 Wirth, R. (2004) Focused Ion Beam (FIB): a novel technology for advanced application of
887 micro-and nanoanalysis in geosciences and applied mineralogy. *Eur. J. Mineral.* **16**, 863–876.

888 Wirth, R. (2009) Focused Ion Beam (FIB) combined with SEM and TEM: Advanced
889 analytical tools for studies of chemical composition, microstructure and crystal structure in
890 geomaterials on a nanometre scale. *Chemi. Geol.* **261**, 217–229.

891 Wu, Z., Peacock, C.L., Lanson, B., Yin, H., Zheng, L., Chen, Z., Tan, W., Qiu, G., Liu, F.,
892 Feng, X. (2019) Transformation of Co-containing birnessite to todorokite: Effect of Co on the
893 transformation and implications for Co mobility. *Geochim. Cosmochim. Acta* **246**, 21-40.

Figure captions:

Figure 1: Bathymetric map of the eastern German contract area with locations of nodules studied here (from Kuhn et al., 2015).

Figure 2 a: Backscattered electron (BSE) map of individual layer growth structures (LGS) of a Mn nodule from the sediment surface (SO205-32KG, 3 μ m beam size). **b-f:** Element distribution maps of individual LGS of the surface nodule shown in a. Based on Mn and Fe, two distinct LGS can be recognized: Mn-rich LGS of suboxic origin and Fe-rich LGS of hydrogenetic origin. Copper and Ni are more strongly enriched than Co in the Mn-rich LGS. Cobalt is more highly enriched in Fe-rich areas.

Figure 3 a: Backscattered electron (BSE) map of layer growth structures (LGS) of a deeply buried Mn nodule (SO240-22KL-801cm, 5 μ m beam size). The red square marks the magnification of the Fe-rich LGS in figure 4. **b-f:** Element distribution maps of individual LGS of the deeply buried Mn nodule shown in a. Here Mn and Fe are well fractionated. The Fe-rich LGS is completely depleted in metals (e.g., Ni, Cu, Co). Metals are associated with Mn at the rims of the suboxic-diagenetic dendritic LGS. Co is also enriched to suboxic-diagenetic LGS.

Figure 4: BSE image magnification of the red square area in figure 3a. The Fe-rich LGS is not homogenous but rather a mixture of remaining hydrogenetic material that is in a different state of dissolution than the suboxic-diagenetic LGS and the newly formed Fe-rich phases.

Figure 5: XRD patterns of Mn nodules from the sediment surface (21KG) compared with nodules which are buried in shallow (subsurface: 14 – 16 cm) and deep sediment (>530 cm). All nodules were analyzed after drying at 40°C (black pattern) and 105°C (grey pattern) causing the differences in the diffraction pattern at the same intensity level. Stars (*) indicate other minerals such as feldspar, quartz and phillipsite.

Figure 6 a: High Resolution Transmission Electron Microprobe (HRTEM) image of the dendritic growth structure close to the Fe-Si-Al LGS area, where the foil comes from is marked as a red square in figure 3a. **b:** HRTEM image of dendritic LGS within buried nodule 22KL-801cm. Different mineral phases can be recognized such as phyllo-manganates and tectomanganates.

Figure 7: IR spectra of three surface nodules, two subsurface nodules and four deeply buried nodules, from 2200 to 400 wavenumbers [cm^{-1}]. The arrows mark the IR bands that are characteristic for manganate oxides (phyllo-manganate and todorokite). Deeply buried nodules show an additional broad band at $\sim 760 \text{ cm}^{-1}$ that is typical for tunnel manganese oxides (todorokite) and is absent in surface nodules.

Figure 8: Ni *K*-edge EXAFS spectra (a) and their respective Fourier transformed (FT) EXAFS measurements (b) of surface, subsurface and deeply buried nodules. The peaks indicated by the arrows between 6 and 7 k \AA^{-1} (a) show the changes between surface and deeply buried nodules.

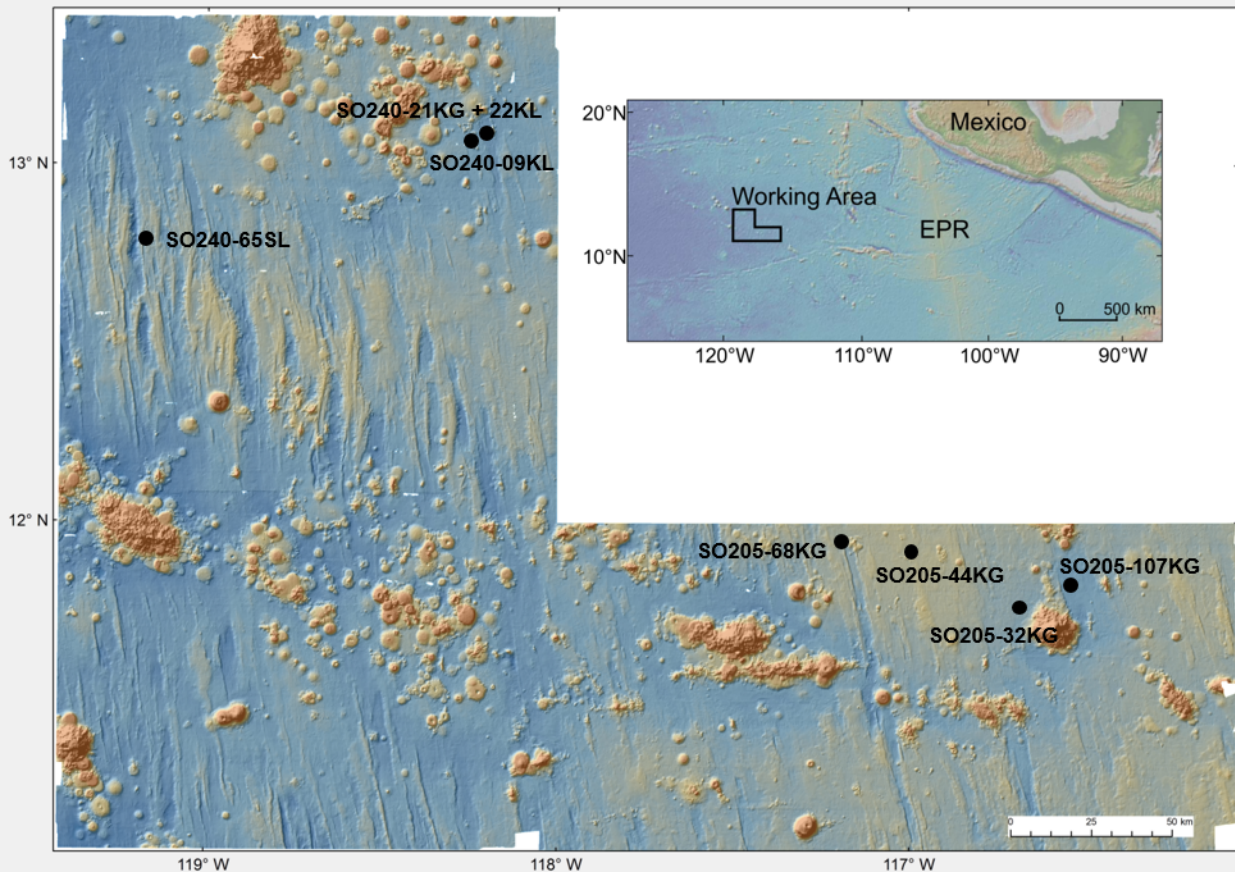
Figure 9: Cu *K*-edge EXAFS spectra (a) and their respective Fourier transformed (FT) EXAFS measurements (b) of surface, subsurface, and deeply buried nodules. The arrows between 5 and 6 k \AA^{-1} (a) mark the changes between surface and deeply buried nodules. Deep buried nodules only show one oscillation, which is the first shell around the Cu atom (oxygen; Cu-O binding). **b:** The intensity of the peak around 2.45 \AA (Cu-Mn) decreases with increasing sediment depth where nodules were buried.

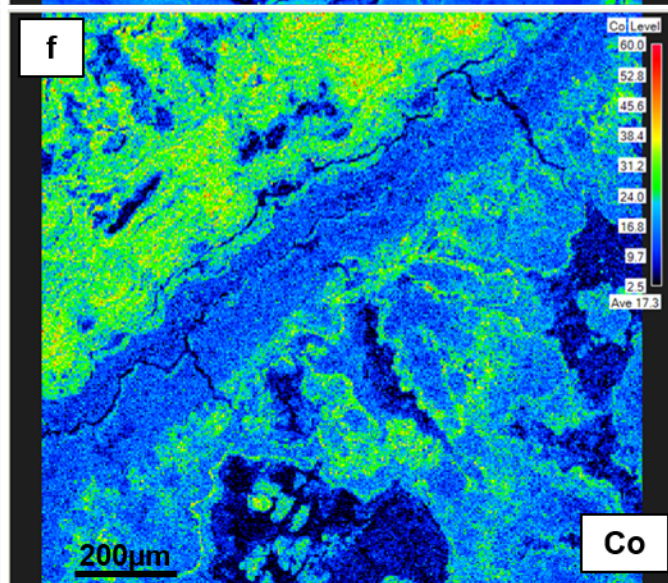
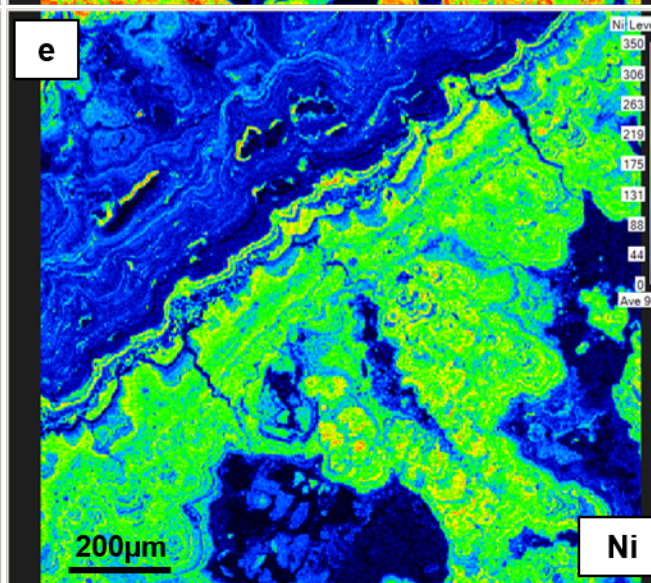
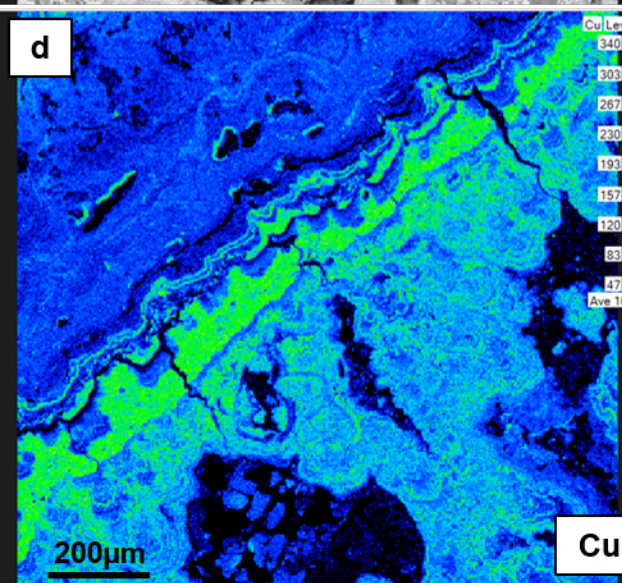
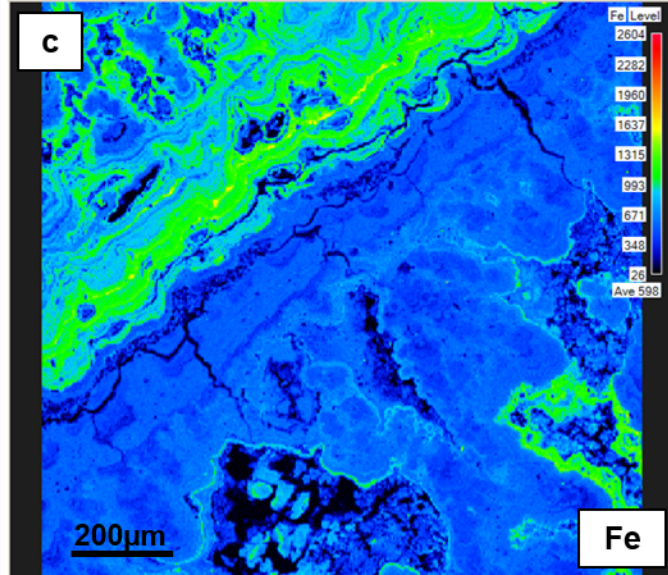
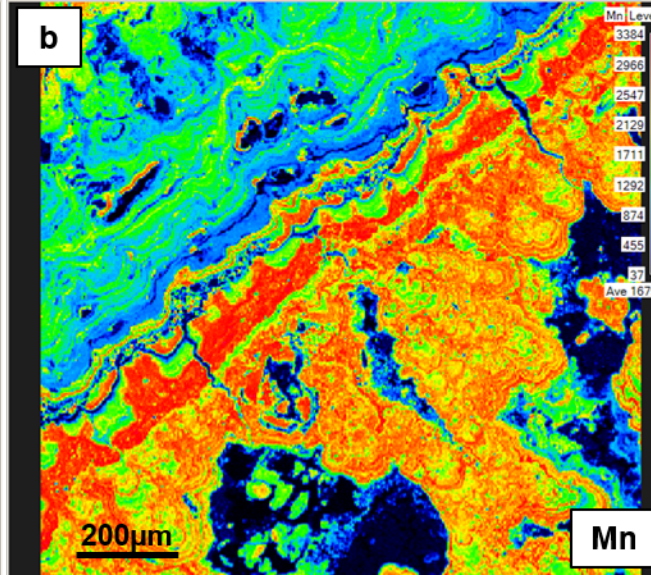
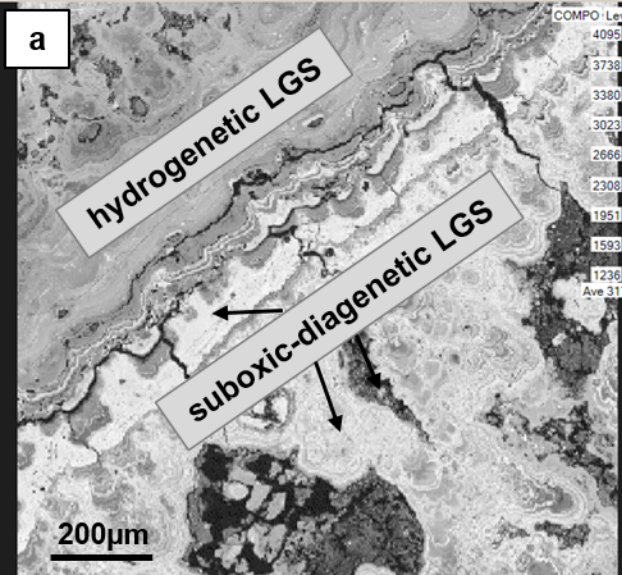
Figure 10: Co *K*-edge EXAFS spectrum (a) and Co Fourier transformed (FT) EXAFS measurement (b) (data show a merge of different measurements) on Co-rich suboxic-diagenetic layer growth structures of a deeply buried nodule (SO240-22KL-801cm).

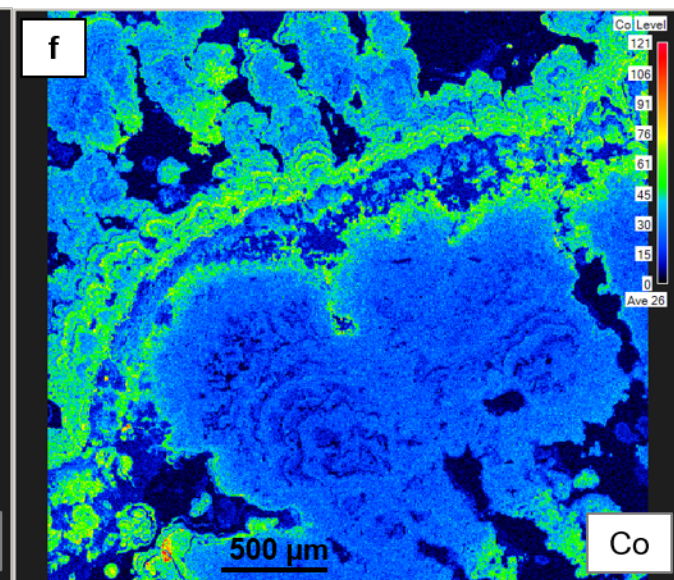
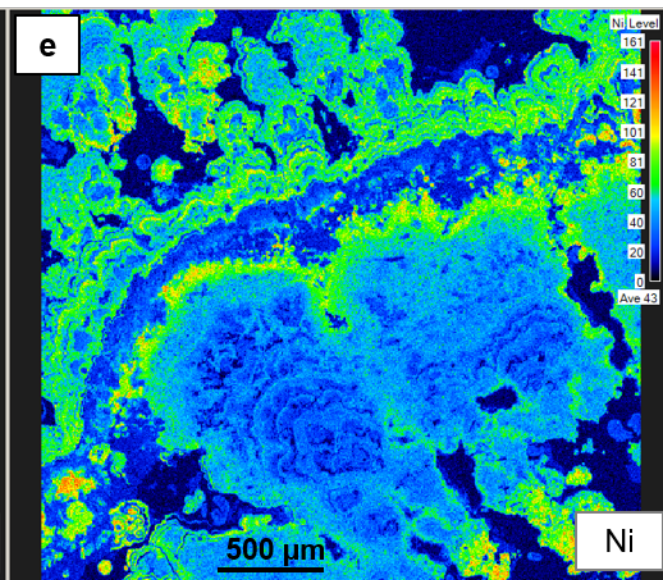
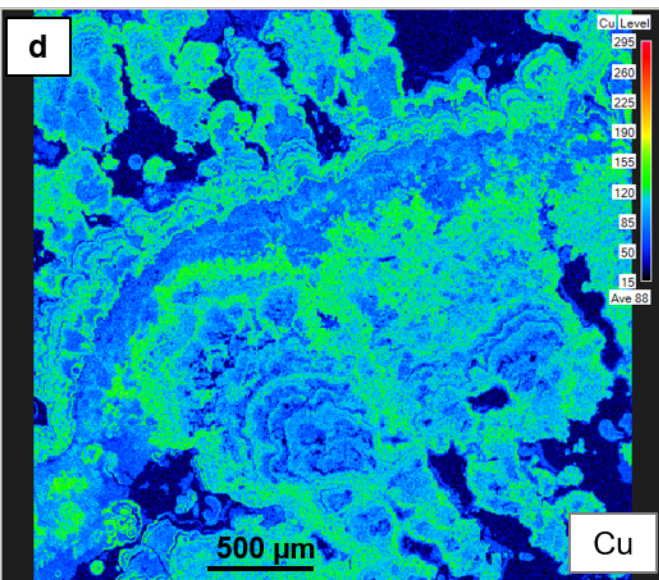
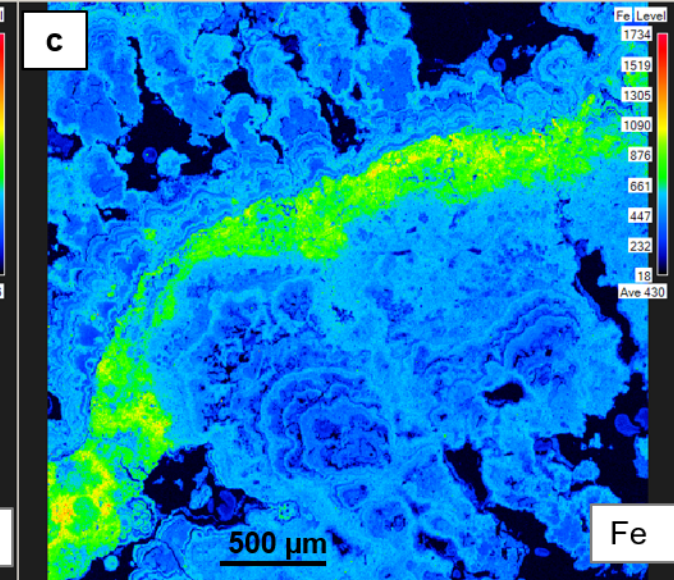
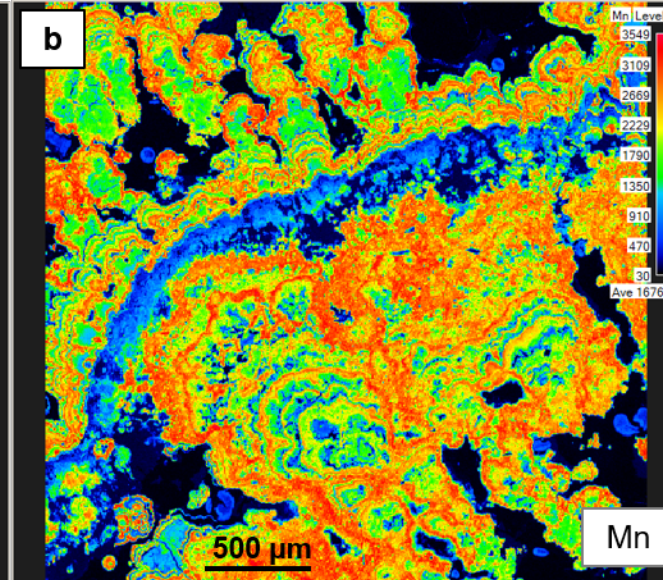
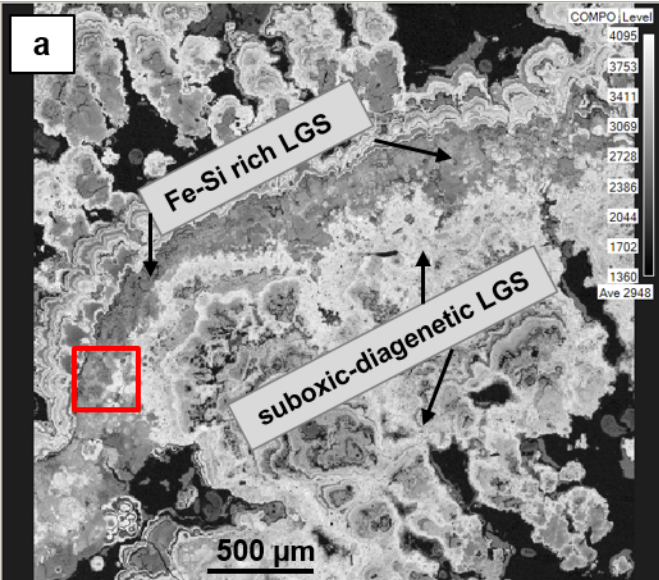
Figure 11 a: Comparison between Ni and Cu Fourier transformed (FT) EXAFS measurements of a nodule from the sediment surface (21KG). The amplitude of the second peak (Ni-Mn) of Ni FT is more intense than that of Cu FT (Cu-Mn), which results from the difference of the number of neighbor atoms around the metal (Ni or Cu). Higher amplitude is characteristic for more neighbors (b). **b:** Model of incorporation of Ni and Cu in the $[\text{MnO}_6]$ -octahedral sheets of phyllosulfates of surface nodules. Only the incorporation of Ni and Cu is shown in the model because the proportion of Cu and Ni sorbed as triple-corner sharing complexes versus vacancies in phyllosulfates is very small.

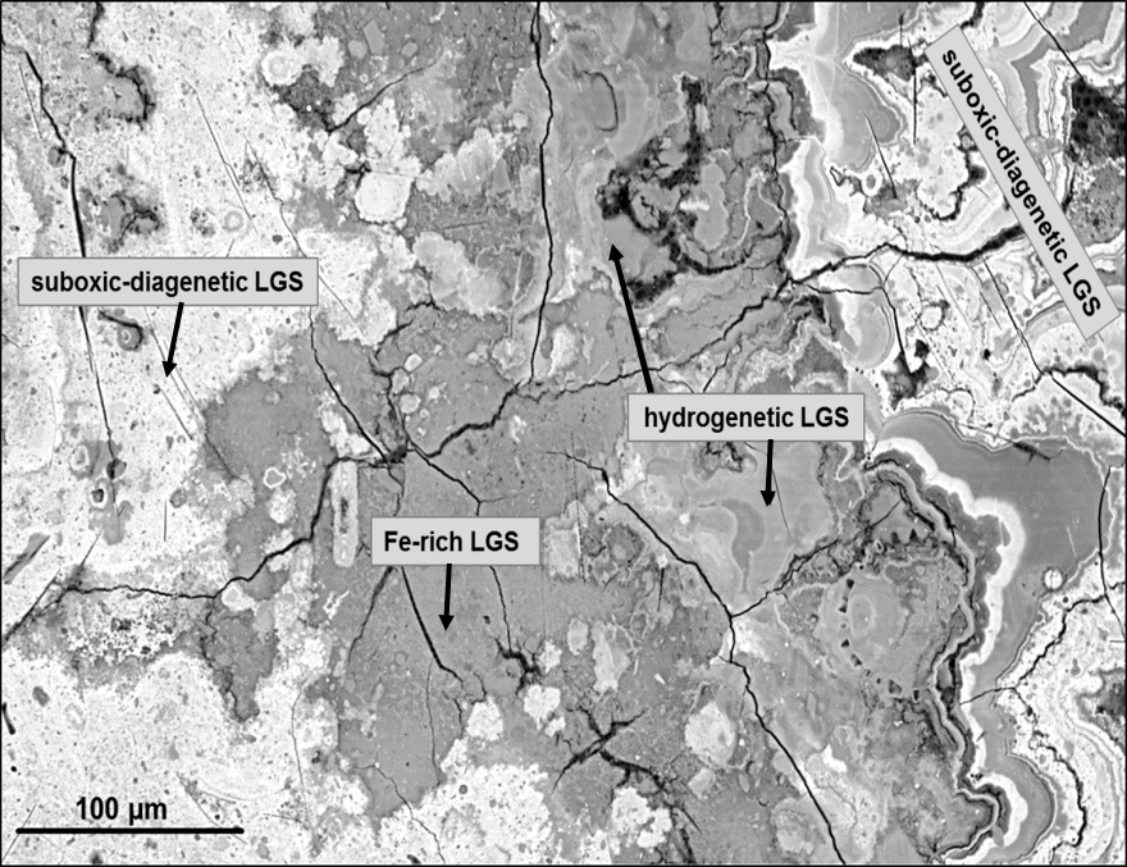
Figure 12 a: Comparison between Ni and Cu Fourier transformed (FT) EXAFS measurements of a deeply buried nodule (65SL-985cm). The amplitude of the second peak of Ni FT (Ni-Mn) is more intense than that of Cu FT (Cu-Mn) due to the higher number of neighboring atoms. **b:** Model of the incorporation of Ni, Cu and Co into the todorokite structure of deeply buried nodules. Ni and Co can be incorporated in the middle of the three octahedra chains of the todorokite tunnel, minor amounts of Ni can be also incorporated on the edges of the octahedra chains. Cu and Ni can also be located as outer-sphere complex within the todorokite tunnel structure.

Figure 13: Cu *K*-edge EXAFS spectra of surface, subsurface and deeply buried nodules compared with different Cu *K*-edge EXAFS measurements of Manceau et al. (2014). The arrow at 5.5 k \AA^{-1} mark the differences between the individual samples. **b:** Cu FT EXAFS measurements of surface, subsurface, and deeply buried nodules compared with data of Manceau et al. (2014).









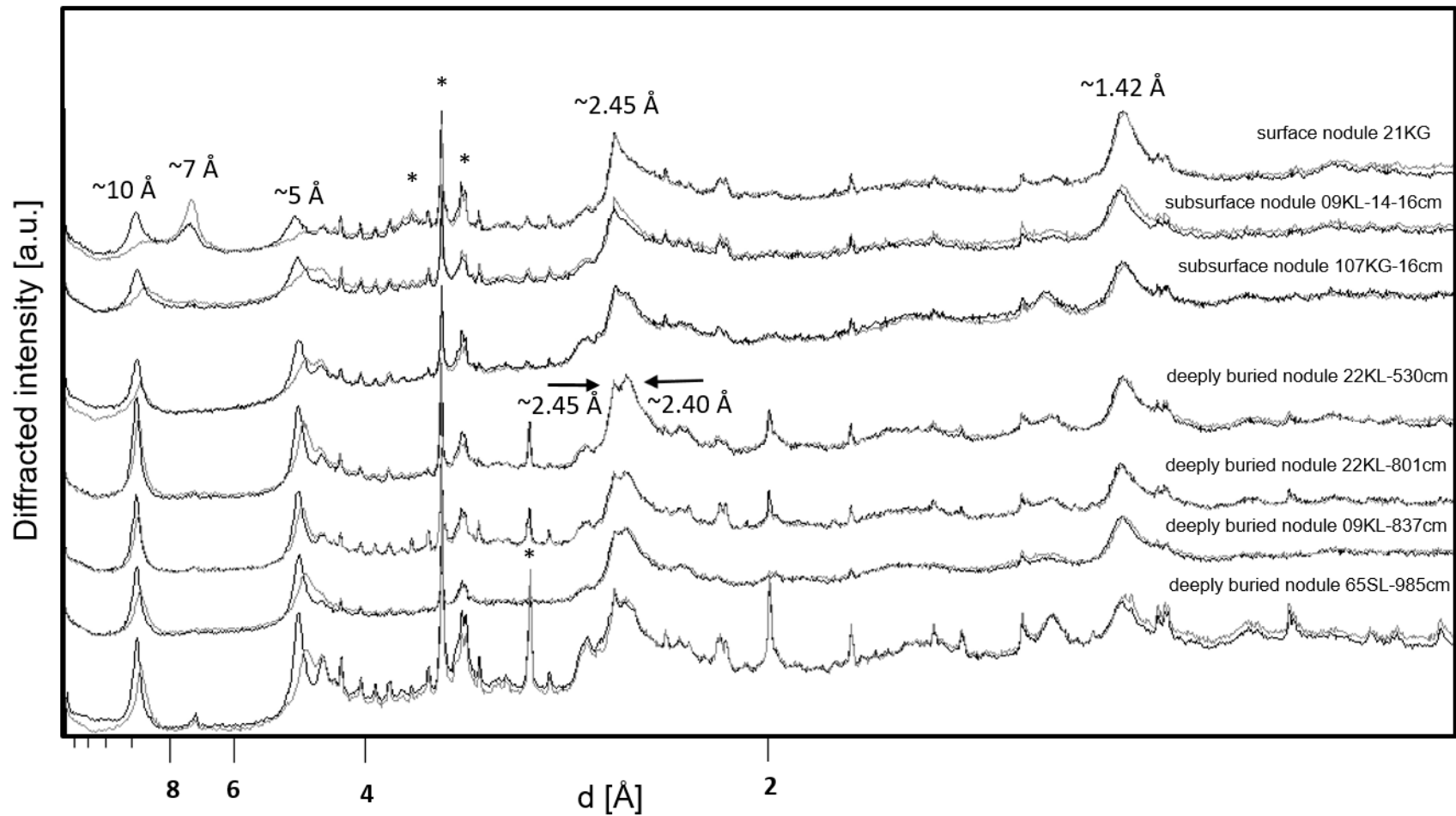
suboxic-diagenetic LGS

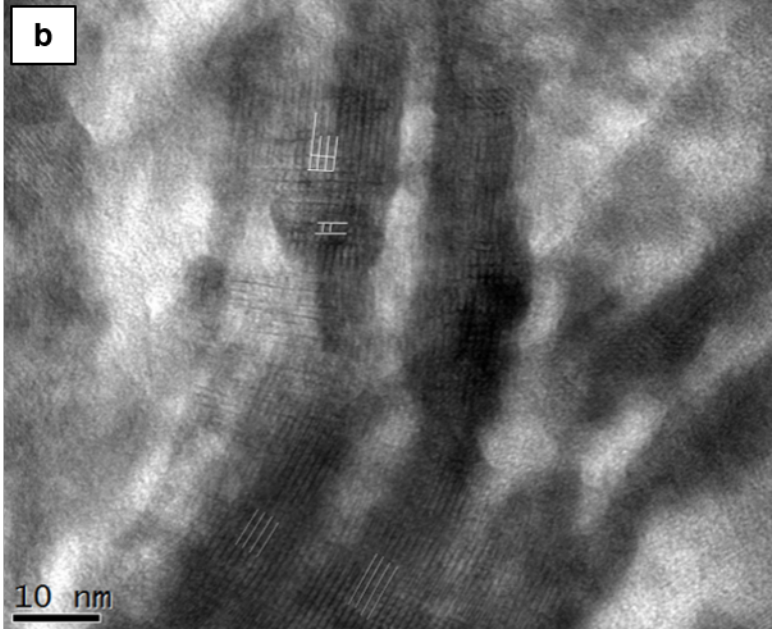
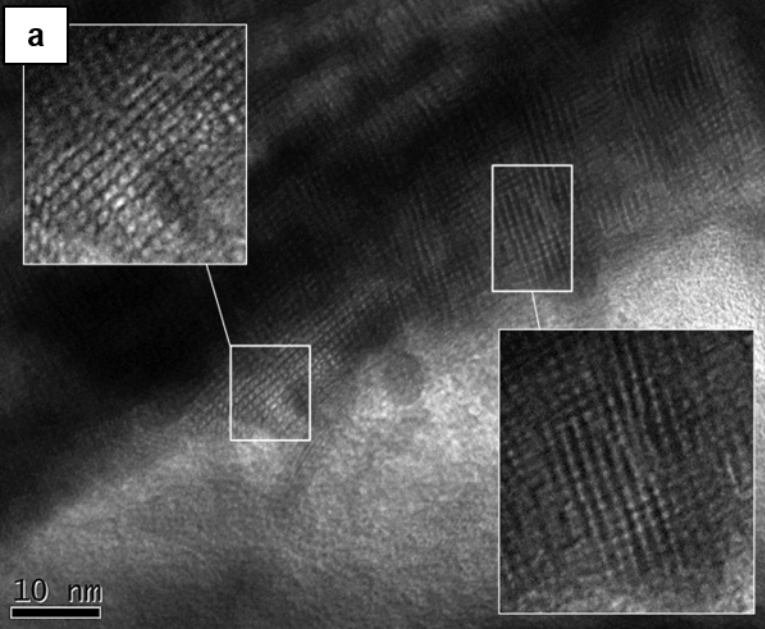
suboxic-diagenetic LGS

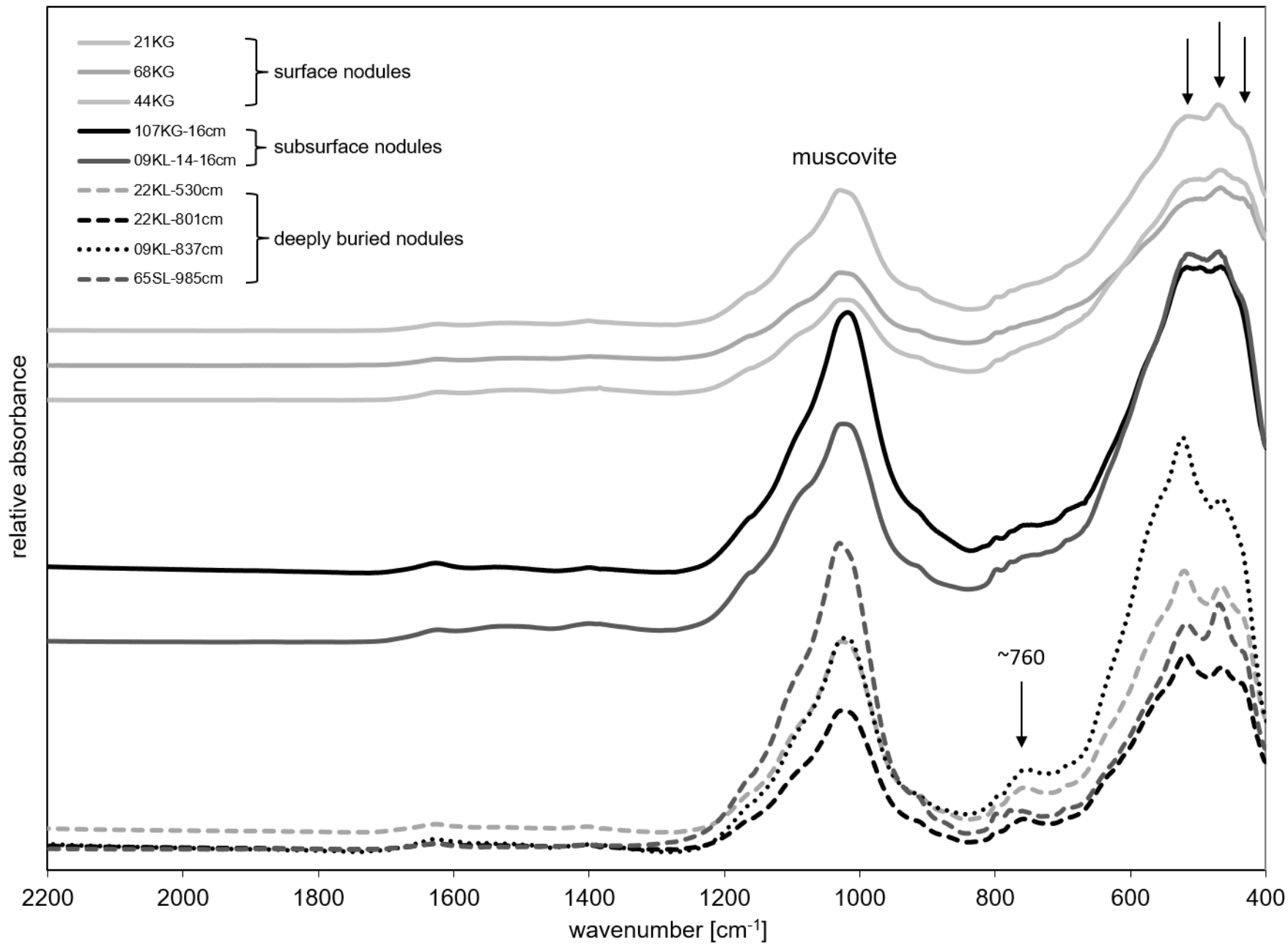
hydrogenetic LGS

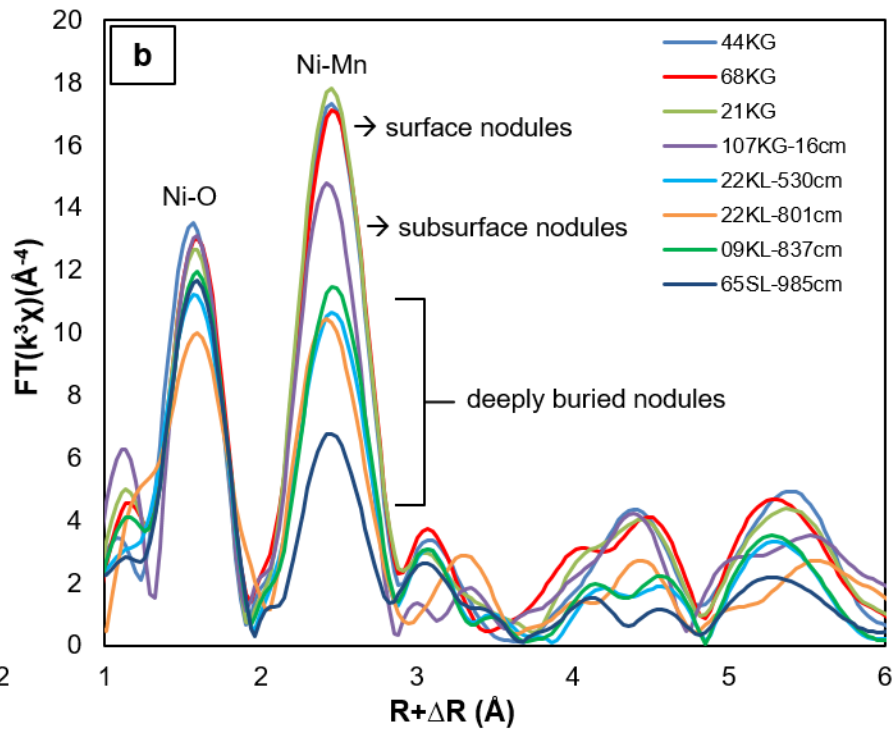
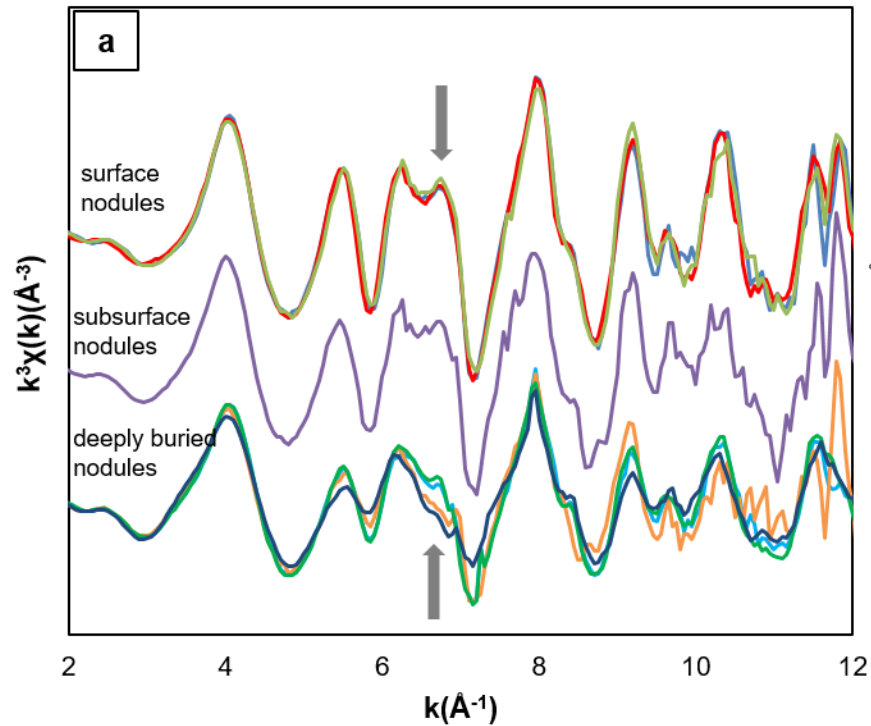
Fe-rich LGS

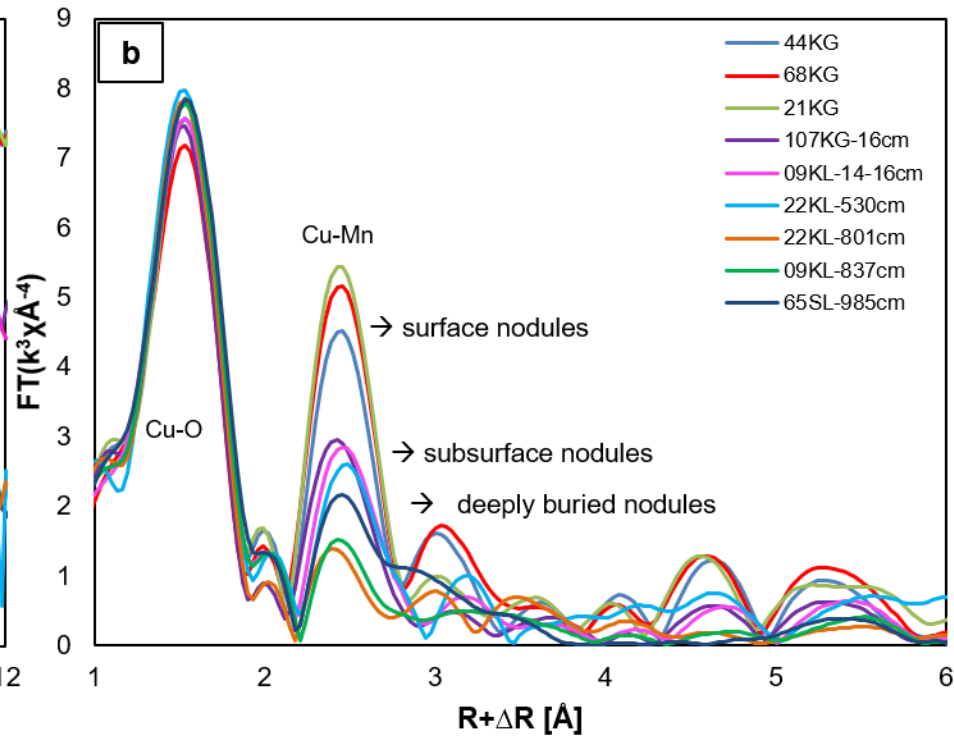
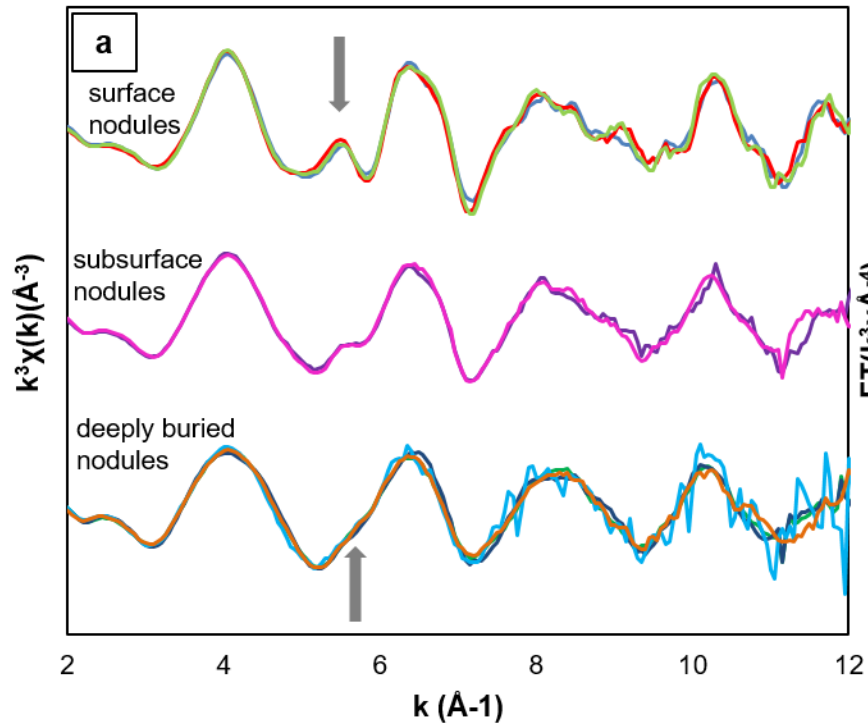
100 μm

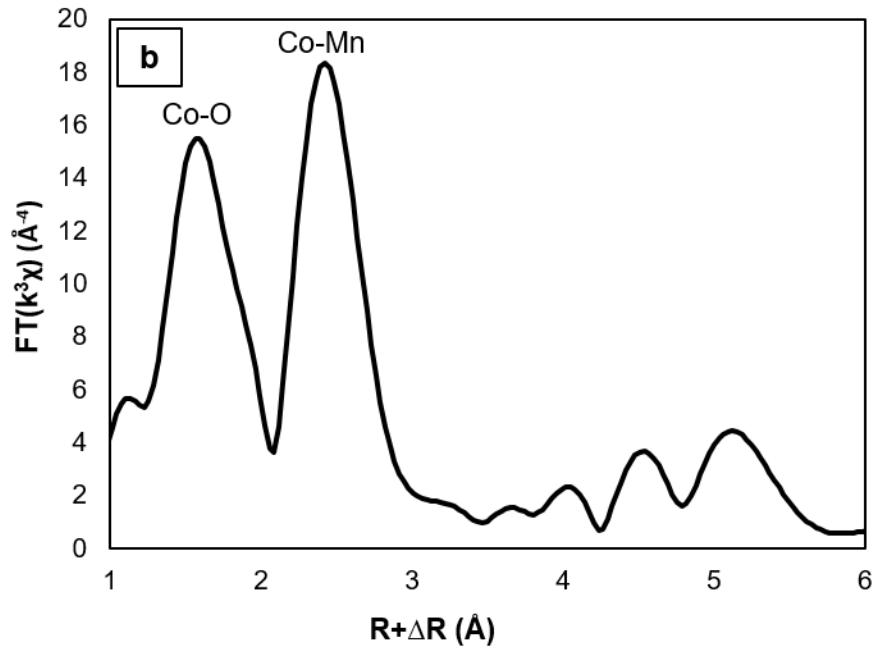
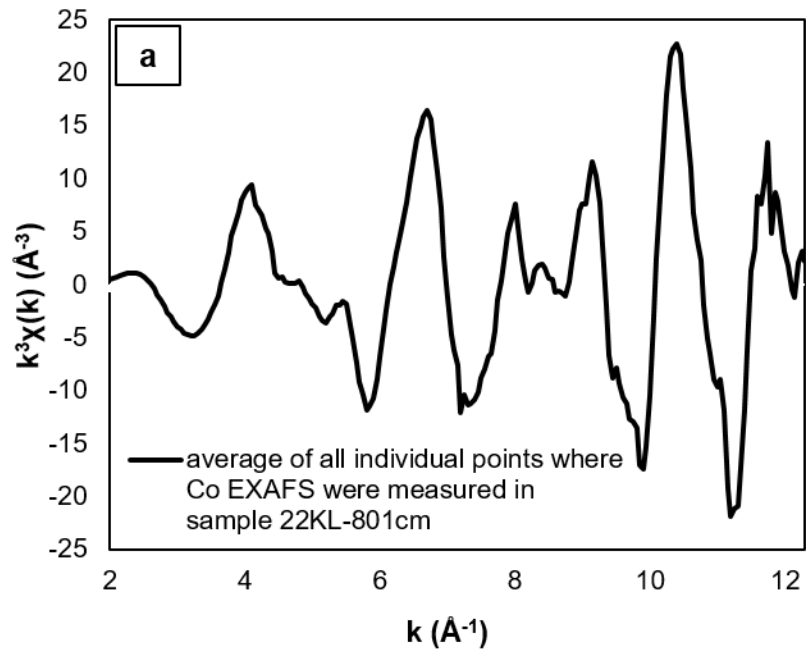


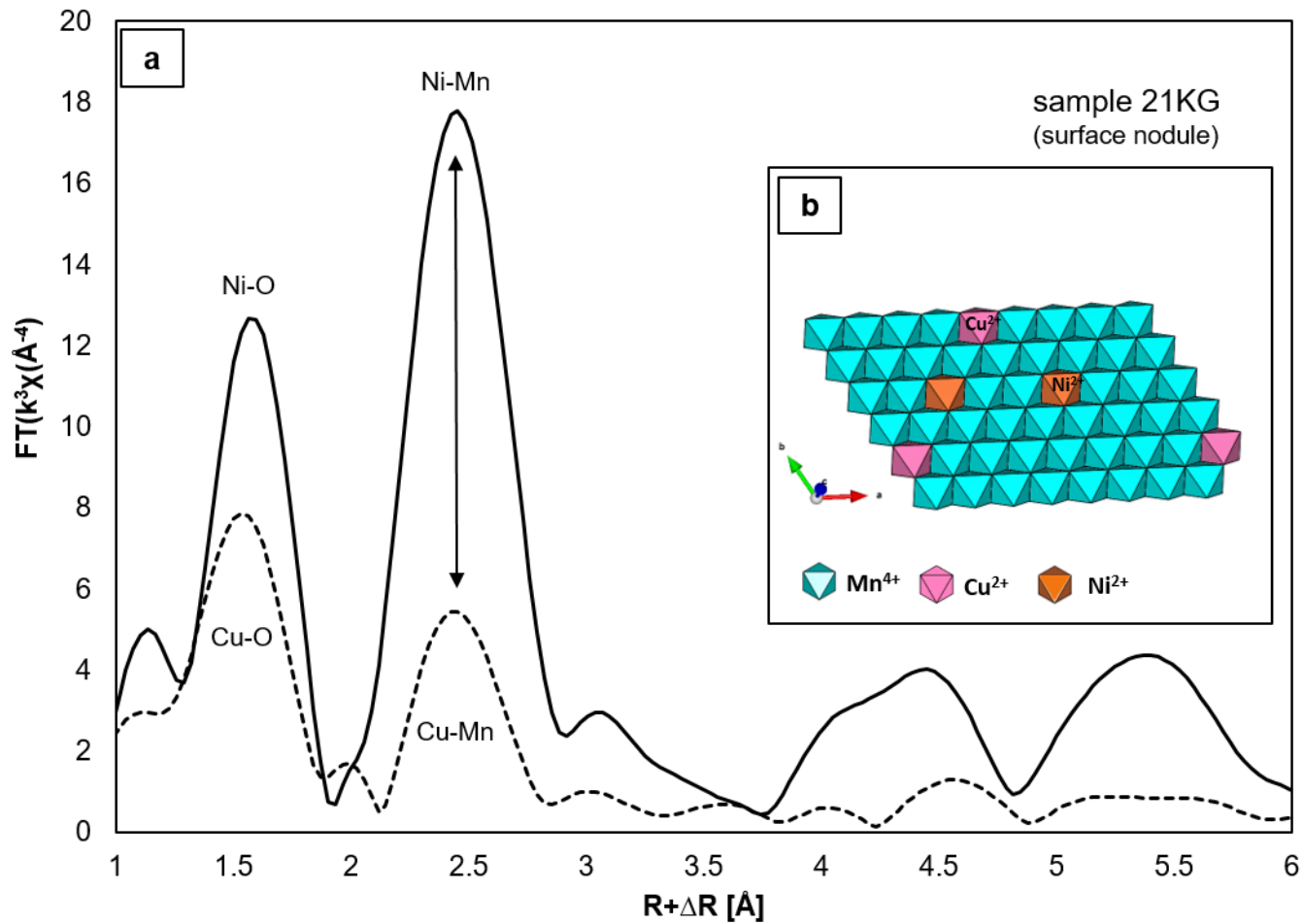


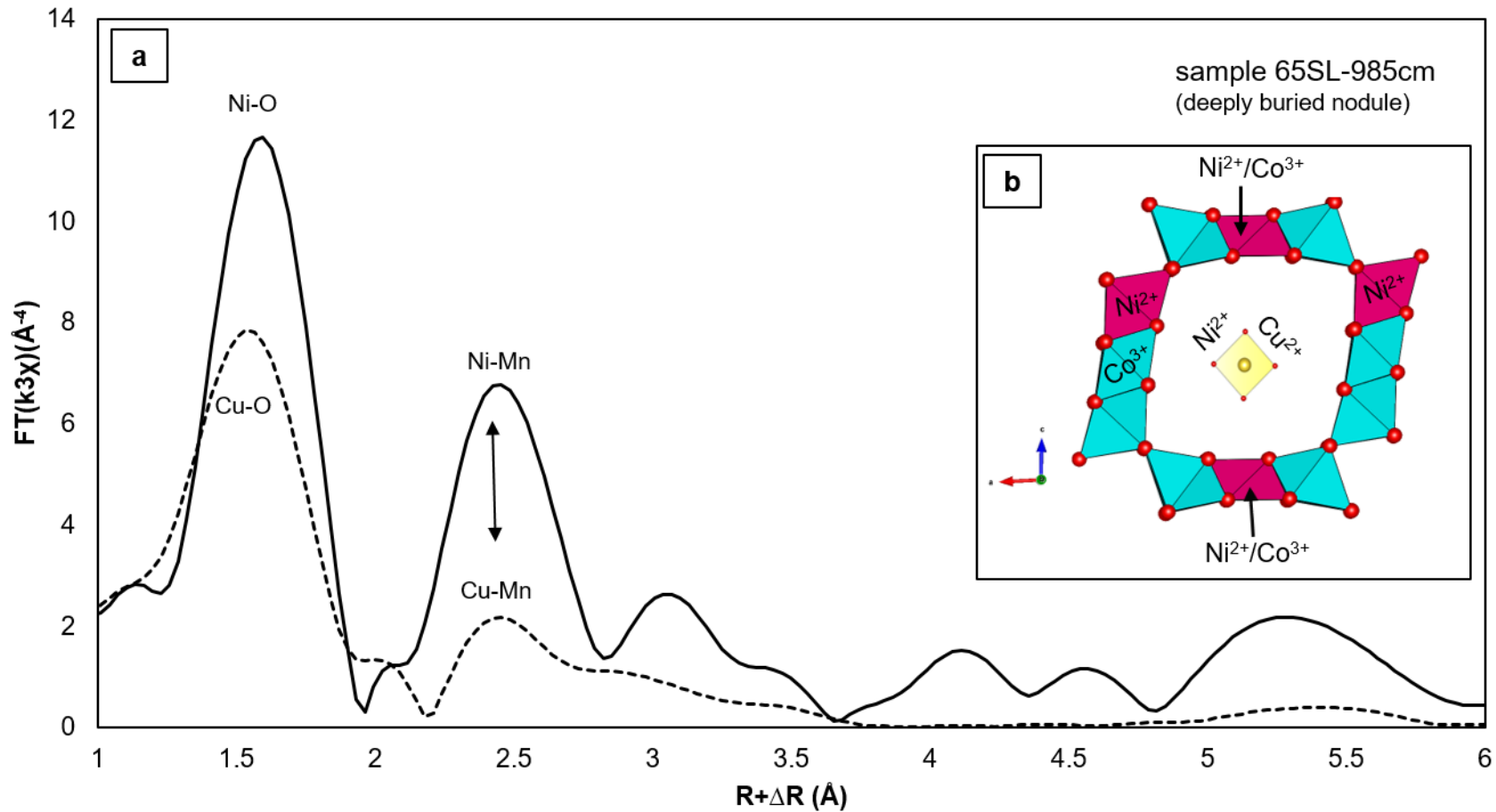












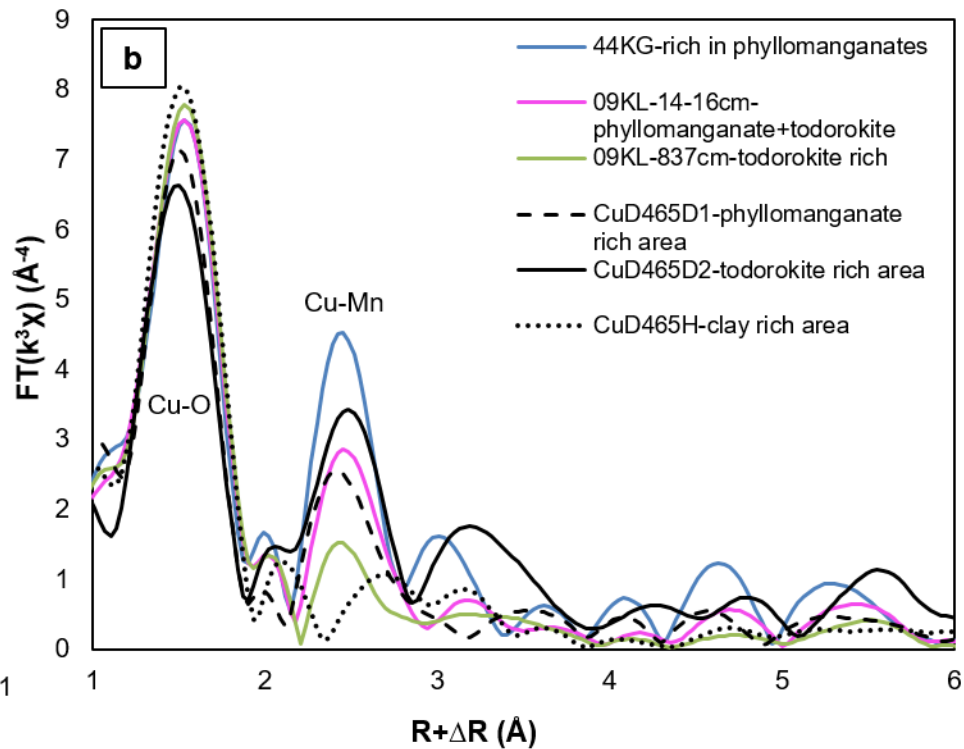
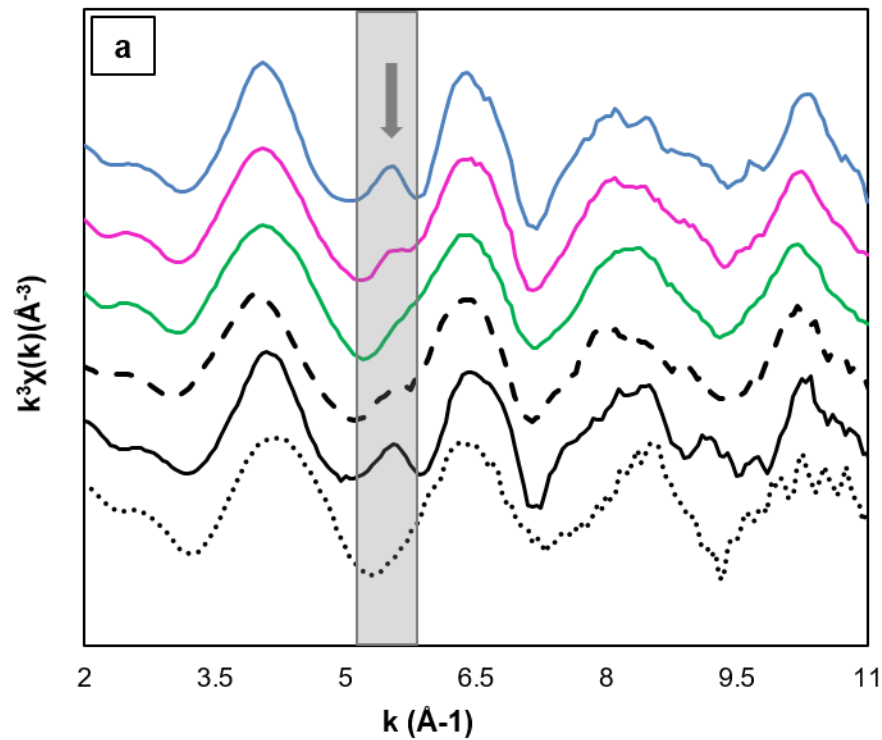


Table 1: EXAFS fits for Ni in surface, subsurface and deeply buried bulk nodules from the CCZ.

sample	nodule location	shell	R (Å)	$\delta^2(\text{Å}^2)$	CN	E (%)	TC(%)	E_0 (eV)	R-factor
44KG	sediment surface	Ni-O	2.01	0.003	6.0	85	15	-4.55	0.02
		Ni-Mn (E)	2.84	0.004	5.1				
		Ni-Mn (TC)	3.49	-0.001	0.9				
68KG	sediment surface	Ni-O	2.03	0.004	6.0	100		-0.31	0.02
		Ni-Mn (E)	2.87	0.004	6.0				
21KG	sediment surface	Ni-O	2.03	0.004	6.0	100		-0.47	0.02
		Ni-Mn (E)	2.86	0.004	6.0				
107KG-16cm	buried, 16 cmbsf	Ni-O	2.03	0.004	6.0	100		-3.24	0.03
		Ni-Mn (E)	2.86	0.005	5.7				
22KL-530cm	buried, 530 cmbsf	Ni-O	2.04	0.005	6.0	76	24	-0.24	0.01
		Ni-Mn (E)	2.87	0.005	4.6				
		Ni-Mn (TC)	3.57	0.009	1.4				
22KL-801cm	buried, 801 cmbsf	Ni-O	2.05	0.006	6.0	68	32	-0.81	0.06
		Ni-Mn (E)	2.88	0.005	4.1				
		Ni-Mn (TC)	4.00	0.005	1.9				
09KL-837cm	buried, 837 cmbsf	Ni-O	2.04	0.004	6.0	75	25	0.01	0.01
		Ni-Mn (E)	2.88	0.005	4.5				
		Ni-Mn (TC)	3.58	0.010	1.5				
65SL-985cm	buried, 985 cmbsf	Ni-O	2.04	0.005	6.0	35	65	-1.17	0.02
		Ni-Mn (E)	2.87	0.003	2.1				
		Ni-Mn (TC)	3.55	0.016	3.9				

E = edge-sharing complex = metals incorporation into the manganese layer sheets;

TC = triple corner sharing complex = metals adsorption above/below vacancy sites of phyllosilicate sheets;

CN=coordination number; R=binding distance; δ =Debye Weller factor (The Debye-Waller factor describes the attenuation of x-ray scattering or coherent neutron scattering caused by thermal motion. It is temperature dependent and characteristic for individual elements); E_0 =energy shift; R-factor = goodness of fit parameter; cmbsf = centimeters below seafloor

Table 2: EXAFS fits for Cu in surface bulk nodules from the CCZ.

sample	nodule location	shell	R (Å)	$\delta^2(\text{Å}^2)$	CN	E_0 (eV)	R-factor
44KG	sediment surface	Cu-O	1.96	0.004	3.6	-0.80	0.01
		Cu-Mn (E)	2.87	0.007	1.9		
		Cu-Mn (TC)	3.42	0.007	1.3		
68KG	sediment surface	Cu-O	1.96	0.005	3.7	-1.00	0.01
		Cu-Mn (E)	2.87	0.008	2.5		
		Cu-Mn (TC)	3.45	0.008	1.6		
21KG	sediment surface	Cu-O	1.96	0.003	3.3	-0.38	0.01
		Cu-Mn (E)	2.88	0.007	2.6		
		Cu-Mn (TC)	3.45	0.007	0.9		

Table 3: EXAFS fit for Co in individual Co-rich suboxic-diagenetic growth structures of a buried nodule (22KL-801cm) from the CCZ.

sample	nodule location	shell	R (Å)	δ^2 (Å ²)	CN	E0 (eV)	R-factor
22KL-801cm	buried, 801 cmbsf	Co-O1	1.94	0.001	6.0	1.17	0.02
		Co-O2	2.25	0.001	2.6		
		Co-Mn1 (E)	2.88	0.002	6.0		
		Co-Mn2	3.08	0.002	2.2		